QATAR UNIVERSITY

COLLEGE OF ARTS AND SCIENCES

EFFECT OF ALUMINUM CONCENTRATION ON THE MICROSTRUCTURE AND MECHANICAL PROPERTIES OF NICRCONB HIGH ENTROPY ALLOYS

BY

OMAR ADEL MUSTAFA ABDALLAH

A Thesis Submitted to

the College of Arts and Sciences

in Partial Fulfillment of the Requirements for the Degree of

Masters of Science in Material Science and Technology

January 2023

COMMITTEE PAGE

The members of the Committee approve the Thesis of
Omar Adel Mustafa Abdallah defended on 11/01/2023.

_____
Dr. Khaled Youssef
Thesis/Dissertation Supervisor

_____
Dr. Aboubakr M. Abdullah Ali
Committee Member

_____
Dr. Mohamed Korany Ibrahim Hassan
Committee Member

Approved:

_____
Ahmed Elzatahry, Dean, College of Arts and Sciences

ABSTRACT

ABDALLAH, OMAR, ADEL, Masters : January : 2023, Material Science and Technology

Title: Effect of Aluminum Concentration on The Microstructure and Mechanical Properties of NiCrCoNb High Entropy Alloys

Supervisor of Thesis: Khaled, Youssef.

The debate between growing economies and increased environmental burdens forces countries to make excessive efforts to reduce their energy consumption. The reduction of weight in structural materials, such as Al-based and Ni-based alloys that are utilized in everyday aspects, has a great potential for reducing the consumption of energy and minimizing the burden on the environment. High entropy alloys (HEAs) are a new class of multi-component alloy systems in which the design of the alloys is based not on adding solutes to a single “base” element, but rather on choosing elements that will form solid solutions when mixed with specific concentrations. In this work, we studied the effect of aluminum content on novel NiCrCoNb HEAs and produced low-cost and low-density HEAs with superior unprecedented mechanical properties through simple thermomechanical treatments.

DEDICATION

This Thesis is dedicated to my family for their unconditional love and support.

ACKNOWLEDGMENTS

First, this work would not have been possible without the grace of Allah SWT.

Words cannot explain the sincere gratitude to my mother and father who always supported and motivated me towards knowledge and science.

To Dr. Khaled Youssef, thank you for your genuine kindness, constant encouragement, and kindling my passion for research.

I would like to extend my gratitude to Center of Advanced Materials, Central Laboratory Unity and Qatar Environment and Energy Research Institute for their expertise and assistance in my work.

Lastly, this work was made possible by NPRP Grant no. NPRP11S-1203-170056 from the Qatar National Research Fund.

TABLE OF CONTENTS

LIST OF TABLES

LIST OF FIGURES

CHAPTER 1: INTRODUCTION

The demand for new materials has increased widely as the new technologies of power generation, aerospace, and other applications are required to have a superior material that can save energy and enhance efficiency. High Entropy Alloys (HEAs) are a new novel type of alloys which can deliver outstanding results of strength, structural and corrosion resistance properties. The promising features of HEAs make the idea of replacing the conventional alloys possible, especially in the era that energy saving, and environment protection became a priority for sustainability, wherefore the need of new novel HEAs is required to achieve all declared goals. The quality, efficiency, and reliability of mechanical systems are strongly linked with the type of materials used to construct the device. Many mechanical parts such as engines, turbines, and transmissions must be built from good materials to provide excellent performance. In the fields of power generation, aerospace, and high-speed equipment the material's weight, strength, and thermal stability are the key concepts for resulting a high efficiency and performance. From these requirements, the idea of developing high entropy alloys came to change the concept of the use of traditional alloys by providing more promising features that can save energy consumption and protect our environment. Its well-known that the conventional alloys are typically made from two or more principal components that are chosen based on the needed properties and then other components are added to further improve their properties. The High entropy alloys (HEAs) were initiated in 2004 by Yeh et al. [1] and Cantor et al. [2] individually, where it also named as baseless alloys, compositionally complex alloys, multi-principal element alloys, and concentrated solid solution alloys. In a simple description, HEAs can be defined as alloys that consist of five or more elements which are varied in concentration between 5 to 35 at% [3]. HEAs normally have equiatomic concentration

such as AlCoCrFeNi [4]. Typically, the HEAs are based on the concept that the high entropy of mixing can lead to formation of a stable single-phase microstructure [5]. Since the HEA concept had coined and until the current moment many papers have been published and currently there are a lot of researches are on progress as the scientists believed that HEAs can replace the conventional alloys due to its promising features. It has been reported that HEAs have several exceptional properties such as high hardness and strength [6], high thermal stability [7], and good corrosion resistance [8]. The high entropy super alloys (HESAs) are a batch of high entropy alloys which can provide superior properties epically in high temperature applications such as gas turbines, bearings, and aircraft engines. The microstructure of HESA is similar to the nickel-base super alloy where they consist of γ (FCC) and γ' (L12) phases, and it has been observed an increment in yield strength along with increasing the temperature [9]. Refractory high entropy alloys (RHEAs) are another batch of HEAs which proposed in 2010 by Senkov et al. [10]. The RHEAs are characterized from the other HEAs that its containing refractory elements (Nb, W, Mo, Ta and Re) in their composition where these elements can enhance the properties of the alloy. One of the examples of RHEAs is NbMoTaW which reported to have a yield strength more than 400 MPa at 1600 ºC, and by comparing it to Inconel 718 Ni-base superalloy it give much higher results, as Inconel 718 Ni-base superalloy have a yield strength below 200 MPa at 1000 ºC [10]. These excellent results of RHEAs give a serious indication that it can replace the nickel-base super alloys and take the lead in applications of high-temperature materials. Figure 1 summarized the main classes of HEAs based on the elemental remark [11].

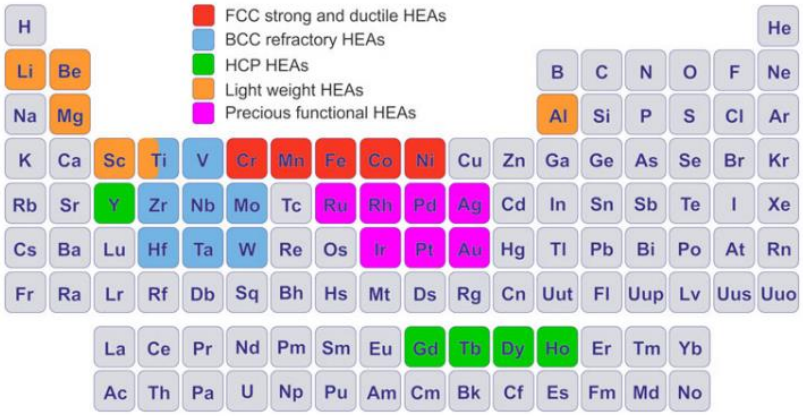

Figure 1: Element groupings highlighting the main ingredients used to synthesize alloys pertaining to the five most typical HEA families.

On this work, we attempt to study the effect of aluminium concentration on the microstructure and mechanical properties of NiCrCoNb high entropy alloy with using several characterization methods where the aluminium concentration will be varied between 0%, 5%, and 10 %.

CHAPTER 2: Literature Review

The subject of understanding the mechanisms and methods of phase stability of HEAs is an active and interesting topic of study for materials science researchers. In 2011 Guo et al. [12] published a research article about the effect of valance electrons on phase stability in HEAs. The authors showed that the elements that tend to produce solid solutions have minimal variations in atomic radius and have almost zero enthalpies of mixing. The little enthalpy of mixing enables the configurational entropy to manage the free energy, where it has been indicated in this case that the system acts more similar as an ideal solution. Otto et al. [13] issued a methodical study on the influence of entropy on the phase stability of HEAs. The research explains that the high configurational entropy is not enough standard to expect if an equiatomic multi-component alloy will produce a single-phase solid solution. Moreover, the article showed that just NiFeCrCoMn alloys can be a single phase fcc solid solution and accordingly a HEA. The results of Guo et al.[12] and Otto et al.[13] were similar where all enthalpies of mixing in the respective binary alloys are comparatively little and the atoms are analogous in size. In their work, the researchers used to replace a single element in an equiatomic NiFeCrCoMn alloy at a time along with elements that own similar atomic size, identical room temperature crystal structure, and similar electronegativity compared to the replaced parts. The rest of the replacements to the NiFeCrCoMn alloy result to a multi-phase alloy. In spite of the replaced elements were analogous in harmoniousness with Hume-Rothery rules, the authors states that the replaced elements had a clearer tendency to produce intermetallics or secondary phases in their corresponding binary alloys. This led the system to act less as an ideal solution, which caused in the creation of a multi-phase alloy with a decreased total entropy [13].

The improvement in technology has raised the demand for new materials that have features fit with the modern technology systems, especially in the defense field of aircraft and power generation equipment. The focal features in these fields are the mechanical properties [14]. The conventional alloys are typically modeled based on a base element such as Fe, Al, and Cu. Still, it found that these elements have a limitation for their properties where it could not be suitable or energy-efficient for the high-performance application. The idea of "High Entropy Alloys" came to solve these issues as this type of alloy can provide interesting features that cannot exist in conventional alloys. High entropy alloy (HEA) is an alloy that consists of five or more elements formed in equimolar ratios [15]. There are also the low entropy alloys (LEAs) which consist of one principal element and the medium entropy alloys, which are composed of 2-4 principal elements [2]. The HEAs have a better hardness at higher temperatures because of the multiple hardening mechanism such as the single-phase solution strengthening, dislocation reaction, and secondary phase strengthening [14]. The interesting point in HEA is that a single-phase structure could result from other elements with different structures [2]. Because of the participation of many elements in producing the HEAs, there is a wide range of HEAs with various structures and properties [15]. The stability of HEAs is typically related to the entropy of mixing (ΔS_{mix}), where the higher entropy of mixing results in a higher stability [14]. So, determining the entropy of mixing is one of the significant rules for obtaining a stable HEA. The valence electron concentration (VEC) is another parameter that plays a rule in determining the crystallinity of the solid solution phase and the type of phase in the absence of a strong atomic size effect [12]. Poletti and Battezzati, and Guo et al. showed in their research papers that the HEAs with a VEC greater than 8.0 give an FCC structure, while the HEAs that have a VEC greater than 6.87 yield BCC structure [12]

[16]. According to Tsai and Yeh review article, the atomic size difference, enthalpy of mixing, entropy of mixing, VEC, and the electronegativity difference are the main factors that influence the formation of binary solid solutions [17].

There are four effects used to describe HEAs; where three of them are hypotheses (high entropy effect, sluggish diffusion effect, and lattice distortion effect) then the fourth one, which is a cocktail effect, is an independent characterization of HEAs [18]. The high entropy effect proposed that the high configurational entropy in almost-equimolar alloys of five or more elements may prefer solid solution phases over intermetallic compounds [15]. The effect of high entropy shows that thermodynamics play a significant part in determining the phases and stability of HEAs. In the lattice distortion effect, a lattice distortion produces from the variation in atom sizes, where the displacement of every lattice site is based on the type of atoms in the local environment and the atom filling that site. In comparing lattice distortion in conventional alloys with HEAs, it has been reported that the lattice distortion in conventional alloys is less than HEAs. Also, it has been reported that the lattice distortion can affect the material properties to increase the hardness and decrease the electrical conductivity, thermal conductivity, and temperature dependence properties [19]. The sluggish diffusion effect proposed that the diffusion in HEAs is slow / almost inactive. The principle of this effect is based on the observation of amorphous and nanocrystals phases over solidification and inspection of the microstructure at the cooling process [1]. The cocktail effect describes three different alloy classes: super-plastic and super-elastic metals (gum metals), bulk metallic glasses, and HEAs [20]. Also, the cocktail effect defines the properties of each alloy class where it states that extraordinary material properties can exist from unexpected interactions.

The main families of the multi-principal element alloys (MPEAs) were classified into seven main categories, which are: refractory metal complex concentrated alloys (CCAs), CCA brasses and bronzes, 3d transition metal CCAs, lanthanide (4f) transition metal CCAs, light metal CCAs, interstitial compound CCAs and precious metal CCAs [15]. The refractory metal CCAs contain refractory elements (Nb, Ta,Hf…etc.), where it is reported that these elements cause enhancement in the material strength [21]. The 3d transition metal CCAs is the most extensively studied alloy, including at least four out of the nine next elements: Fe, Cu, Co, Ni, Al, V, Mn, Cr, and Ti [2].

2.1 Properties prediction and elements selection

The prediction and forecasting of the material properties through modern techniques is the new method of material design as it could save time and raw materials instead of making useless attempts, leading to worthless results. Machine learning (ML) has been wildly used to study the properties of materials [22] where it could effectively infer the relationship between material descriptors and target property through constructing a surrogate model without explicit programming [23]. Guillermo at el. [24] published recently an article reporting machine-learning model for fast assessment of elastic properties of HEAs where they developed descriptor-based analytical models using SISSO-based (sure independence screening and sparsifying operator) machine learning to predict mechanical properties of solid-solutions utilizing a database of elastic properties determined from density functional theory (DFT) for binary and ternary subsets of Nb-Mo-Ta-W-V refractory alloys. The proposed models designed to predict or induce ductility in RHEAs (refractory high entropy alloys) and link it to VEC (valence electron concentration). Guillermo at el. [24] produced in Figure 2 computationally inexpensive analytical ML model facilities quick search of

technologically useful alloys over multidimensional spaces. Their estimates of σ_{0y} in Figure 2a proposes near a region in (Nb-Ta)-(Mo-W)-V compositions space that shows greater strength, which is different from the high entropy of mixing (ΔS_{mix}) region (marked by solid white dot) doesn't necessarily correlate with mechanical or electronic behavior. In contrast to the usual expectations, they found that the region of high yield-strength in Figure 2a directly correlates with higher thermodynamic stability(ΔH_{mix}) as shown in Figure 2b. The inserting point in their research that the improving trends (ML predicted) in yield strength from quaternary NbTaMoW (1.12 GPa) to quinary NbTaMoWV (2.00 GPa) matched with the previous experiments [10] [25], where adding V was found to increase the strength of the alloy. The parabolic area in Figure 2 a, b displays the area of high electronegativity variance ($\Delta\chi_{var}$), it reported that the $\Delta\chi_{var}$ increases with increase in V and Nb/Ta more compared to Mo/W due to the higher V electronegativity compared to others. The authors theorize that the large $\Delta\chi_{var}$ may lead to high charge imbalance in the nearby environment of V as large χ pulls more charge, which adds local lattice distortion and hence provide local solid solution strengthening. The additive of V could be the main reason for the strong correlation between σ_{0y} and ΔH_{mix} in Figure 2 a, b as it enhances the alloy stability and local-lattice distortion as reported by Song et al. [26]. In the end the paper mentioned that the proposed assessment suggests that an optimal combination of entropy, phase stability, and $\Delta\chi_{var}$ results to higher yield strength.

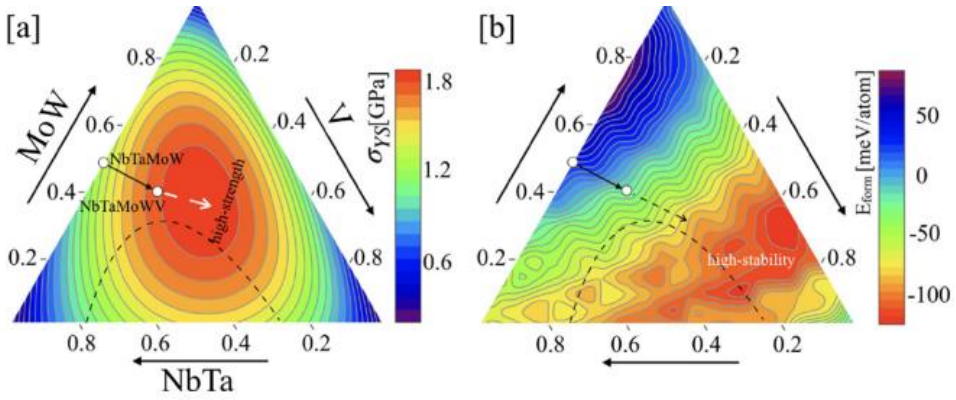

Figure 2: (a) Yield-strength σ_{0y} and (b) formation enthalpy (ΔH at 0 K) vs composition (ci, i=Nb/Ta, Mo/W, V) [24].

2.2 Effect of aluminum concentration on HEAs

It is well-known that the mechanical properties mainly depend on the chemical composition and crystal structure of the material. The mechanical properties such as strength, stiffness, and wear resistance can be changed and manipulated in determining these factors. In 2013 it was reported by Tsai et al that an FCC crystal structure of HEA formed with containing Fe, Cr, Mn, Co, and Ni in a mixture of a total of 20 elements at equiatomic concentration, while a BCC structure of HEA was formed in a composition of AlCrCuFeNiZn, where it has been explained that the formation of the composite of Cr-Fe and Ni-Al was the reason of forming BCC structure [27]. Miracle and Senkov mentioned in their research article that the aluminum concentration in HEAs is one of the most important studies in the field of HEAs, where they reported that the increment of the Al concentration would cause to enhance the tensile strength and reduce the ductility [15]. In addition, the variation in Al concentration plays a role in determining the type of microstructure, where it has been reported that a single-phase FCC exists when the Al concentration is equal to or less than 8%. In comparison, FCC and BCC phases exist when the Al concentration is between 8% and 16% [28]. Moreover, Yeh and his colleagues mentioned in their research paper that an enhancement in hardness of AlxCoCrCuFeNi HEA was recorded with an increment in Al content because of a

phase conversion from single-phase FCC to FCC+BCC and then to single-phase BCC [29]. In another research, Sharma et al. confirmed in their article that adding Al to the HEA $MoCr_{0.5}NbTa_{0.5}ZrTi$ caused to increase in the hardness and density by 12%, while they notice a reduction in the composition's density by 10.1% [14]. Chung at el. reported that Al and Cr are BCC phase stabilizers unlike Ni and Co which working as FCC phase stabilizers [30].

2.3 Mechanical properties of HEAs

The mechanical properties of HEAs can be changed significantly due to the vast number of alloy compositions and the wide range of elements percentages, where the strength of each phase, distribution of phases, and the volume ratio of each phase are the critical factors that could vary with the alterations in the chemical composition [17]. When two HEAs are similar in the relative fraction and strength, the distribution of phases can affect the mechanical properties and make the alloys different in properties even when the hardness and relative fraction are similar between [17]. The relative volume ratio of phases in HEA is highly associated to VEC of the alloy, as the greater VEC leads to form higher FCC phases and fewer BCC phases [17].

2.3.1 Hardness

Hardness is one of the key mechanical properties which can be determined rapidly through Vickers hardness testing. The hardness values of HEAs are normally in the range of 140-900 HV, where these values are depends on the alloy composition and processing technique [31]. Typically, the hardness of the FCC phase range between 100–200 HV [32] and the alloys with a single-phase FCC have ductility in the range of 20 – 60% [33]. The HEAs are divided into strong aging hardening and weak aging hardening, which are based on the effect of annealing treatment [34]. Figure 3 representing the effect of aging temperature on the hardness values, where the red line

is representing the strong aging hardening and the black line is representing the weak aging hardening.

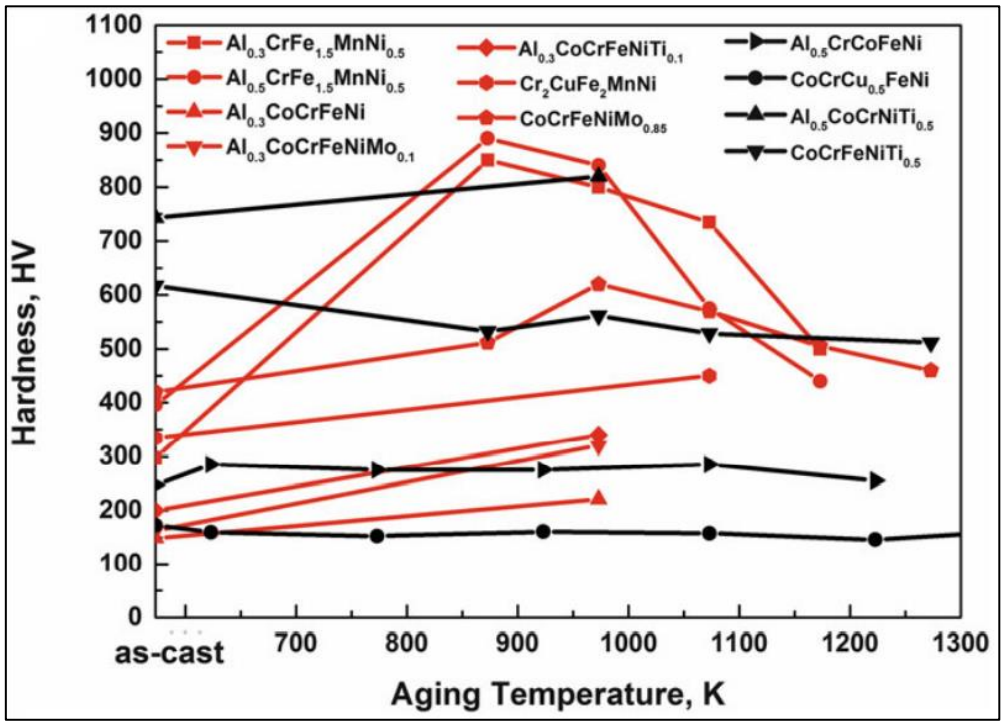

Figure 3: Effect of agening temperature on the hardenss of varoius HEAs [34].

In 2009, Wang and his colleagues studied the mechanical properties of CoCrCuFeNiAl0.5 alloy, which was mainly composed of FCC crystal structure, where they found that the mechanical properties of the sample were 19% of ductility and a minimum of 700 MPa of strength and they mentioned that the alloy sample did not break even at true compressive strength of 50% [35].

The microstructure of HEA can predict the hardness of the material where for each phase the hardness will be typically distributed in certain ranges. The critical stress in FCC phase is typically smaller than BCC phase, and that can be explained because FCC structure has a slip planes with closest packing, also the greater interatomic bonding would provide higher strength [34]. The BCC phase showed to provide higher hardness in several HEAs compositions, such as AlxCoCrCuFeNi [36], AlxCoCrFeNi [37], and $Al_{0.5}$CoCrCuFeNiVx [38]. In addition, the microstructures would influence the

hardness, where the dendritic region in HEA has a different hardness value than interdendritic region [34].

2.3.2 Tensile properties

Tensile test is the main experiment which determine the key mechanical properties of an alloy, such as yield strength, ultimate tensile stress, and ductility. The stress-strain curve of HEAs is greatly influenced by the grain size and structure [34]. Figure 4 is showing an example of the effect of microstructure on tensile properties, where the HEA AlxCoCrFeMnNi was mechanically tested with various Al concentration [28]. The FCC phase noticed to be form in Al0, Al4, Al7, and Al8, this phase was representing higher ductility and lower strength as it reached 63% of ductility. In the other side, the Al9, Al10 and Al11 showed multi-structure of BCC+FCC, where the strength indicated to be much higher but with less ductility. The effect of grain size on the mechanical properties was reported by Otto at el. [39], where they stated that the reduction in the grain size caused to improve the strength of CoCrFeMnNi HEA as shown in Figure 5. From Figure 5, the reduction in grain size improves the composition strength even at elevated temperatures, where its clearly shows a mechanical properties enhancement at all temperatures which has been tested at bigger grain (155 μm) size then at smaller grain size (4.4 μm).

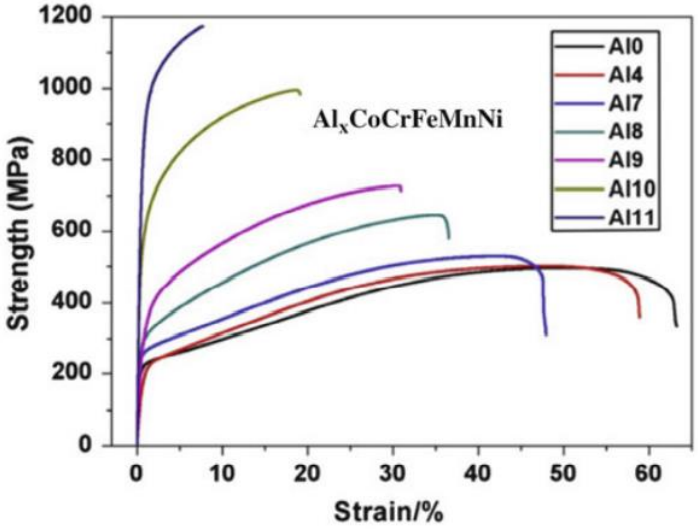

Figure 4: Engineering stress-strain curves of AlxCoCrFeMnNi HEAs (as cast) at different Al concentrations [28].

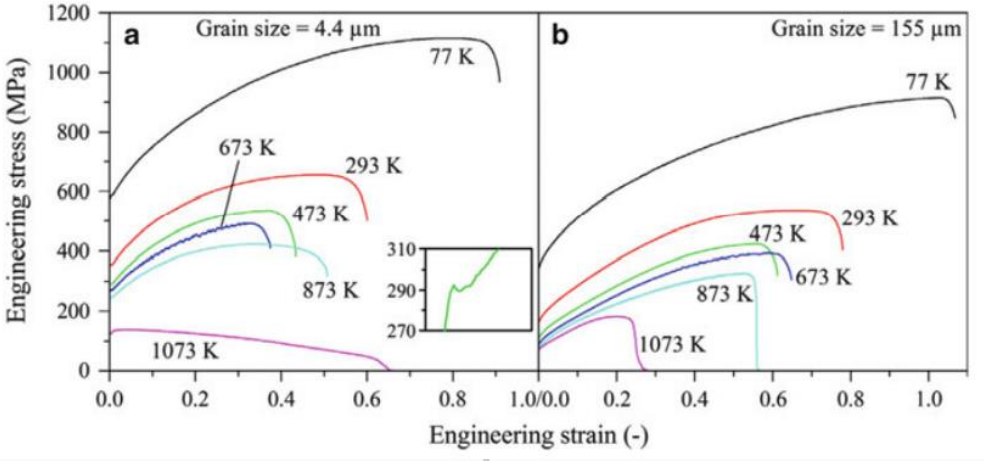

Figure 5: Engineering stress-strain curves of CoCrFeMnNi alloy at different testing temperatures and grain sizes of 4.4 μm and 155 μm [39].

The mechanical properties can be degraded due to defects which includes pores, residual stresses, and casting segregation. In order to obtain a balance between ductility and strength, several methods such as thermo-mechanical processing and thermal treatment are used to accomplish this balance [15].

2.4 Mechanical properties at elevated temperatures

Typically, the increment in temperature causes a strong reduction in the yield stress of the metals which make the material unsuitable for high temperature

applications. As mentioned before in the introduction section, there are many applications that operate at elevated temperatures, and it required to have a unique material which can be stable among high temperatures, and it can maintain its mechanical properties from any changes due to the applied conditions of high temperature and pressure. Figure 6 is summarizing the relation between yield strength and temperature of several HEAs [34]. The curves showed that the yield strength decrease as the temperature increase, but the only difference between all HEAs is how much the decrement in yield strength will be compared to the temperature. The HEA $Al_{0.5}$CoCrCuFeNi (cold-rolled) showed the highest yield strength values in elevated temperatures and CoCrFeMnNi with 155 µm grain size showed the lowest yield strength values in the elevated temperatures.

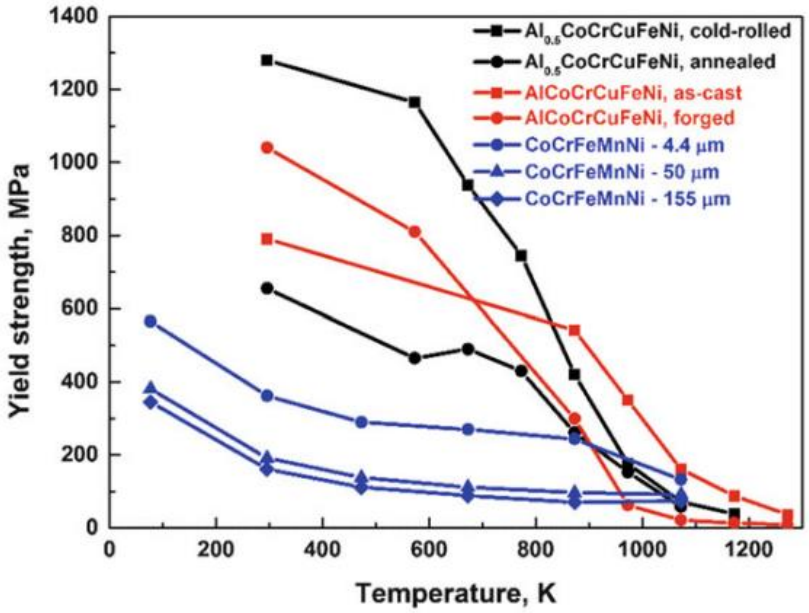

Figure 6: Effect of temperature increment on yield strength for $Al_{0.5}$CoCrCuFeNi, AlCoCrCuFeNi, and CoCrFeMnNi HEAs [34].

The superalloys such as Hastelloy and Inconel are mainly consist of γ and γ' phases, and it characterized that the yield stress increase with increasing the temperature normally up to 1073 ºK (the peak of flow stress) and after this temperature the yield stress will

be decreasing rapidly due to the fast dissolve of γ' phase [3]. This phenomenon can be explained that the strength of γ' is proportionally related to the temperature, as it formed by thermally prompted cross-slip of dislocations from the octahedral {111} plane to cube plane {100} within γ' phase [119]. This special feature has been observed in several HESAs such as $Al_{7.8}Co2_{0.6}Cr_{12.2}Fe_{11.5}Ni_{40.7}Ti_{7.2}$ and $Al_{10}Co_{25}Cr_8Fe_{15}Ni_{36}Ti_6$ [40] [41]. To obtain this phenomenon, the material should have relatively high volume fraction of γ' phase where the decrement in this phase could cause to diminish this phenomenon [3].

2.5 Corrosion properties of HEAs

Corrosion is one of the biggest challenges for metals and alloys as it can reduce the life of the alloy and degrade its mechanical properties to a level where it becomes unsuitable for use. The corrosion resistance has been tested for several HEAs in the solutions H_2SO_4 and NaCl, where it was found that these HEAs had better corrosion resistance than 304SS and 304L SS [42]. Several factors make the HEAs a corrosion resistance material, which are: the microstructure and alloy composition, the presence of galvanic corrosion, and the quantity and spreading of corrosion resistant elements [17]. The corrosion resistance of CoCrFeNi single-phase FCC alloy has been tested in NaCl solution. The researchers found that the sample presents a better corrosion resistance than 304L SS due to the high content of Ni and Cr [43]. On the other hand, the addition of a half mole of Al to CoCrFeNi alloy can lead to forming (Al, Ni)-rich BCC phase, which produces galvanic corrosion in the NaCl solution [44]. Moreover, it has been reported that the addition of aluminum in $AlXCrFe_{1.5}MnNi_{0.5}$ alloy caused a reduction in the corrosion resistance of the alloy due to that the Al typically increases the area of localized/pitting corrosion and reduce the pitting potential of the alloy in NaCl solution [45].

2.6 Thermodynamic approach and phase formation in HEAs

Thermodynamics and kinetics are main keys in designing and developing a stable HEAs, where these concepts considered as the base knowledge of HEAs formation. It has been reported that a thermodynamics methods of CALPHAD (calculation of phase diagram), semi-empirical rules, and ab initio methods have been used in designing HEAs [34]. In the absence of the kinetic factors in the phase formation of HEAs, the phase formation will be controlled through thermodynamics principles, where the Gibbs free energy (G), enthalpy (H), and entropy (S) are the main thermodynamical factors and they expressed in a single equation as shown in the equation 1. The interesting point about this equation that it shows the entropy of mixing (ΔS_{mix}) can significantly reduce Gibbs free energy at elevated temperatures, which will reduce the tendency of order and segregate during solidification, and hence the solid solution will be more easily to form and further stable [34].

$$\Delta G_{mix} = \Delta H_{mix} - T\Delta S_{mix} \qquad \text{equation 1}$$

The atomic size or in general the geometry effect is another factor that plays role in the phase formation of HEAs where this factor has been described through Hume-Rothery rules for forming binary solid solutions [46]. The challenge in the theoretic thermodynamic understanding of HEAs is to find the right incorporation of all competing properties which required a proper qualitative and quantitative understanding [47]. The Gibbs energy (G) is the norm of stable phases in alloys as the reduction of Gibbs energy (G) could cause a formation of a stable phase [48]. One of the methods to design HEAs through thermodynamics approach is to use the phase diagram of binary alloys, as these diagrams can forecast the stable phases that it could produce from certain elements [47]. The method of inspection binary G-x (Gibbs energy – composition) plots has been reported as an useful method to design HEAs

[49]. Figure 7 demonstrates the phase selection diagram based on relation between enthalpy of mixing ΔH_{mix} and atomic size difference (Delta – δ). The graph includes HEAs and BMGs (Bulk metallic glasses). In zone labeled as S, just disordered solid solution will form where it can be noticed that the atomic size difference (δ) is relatively low, and the composition atoms are similar in properties to easily substitute for each other and occupy the lattice sites to form solid solutions. In the other side, the ΔH_{mix} in zone S is not negative enough for alloys to form a compound. In zone S', solid solution is still form as main phase for HEAs with a small amount of ordered solid solution precipitates in some HEAs [34]. The increase in δ at zone S' increase the extent of ordering in HEAs and the decrement in ΔH_{mix} (becomes more negative) assist to promote the precipitation of ordered phases in certain HEAs. The zones B1and B2 are representing the BMGs, where B2 contains Cu and Mg based BMGs and B1 include other kinds of BMGs such as Zr based BMGs. By comparing HEAs with BMGs, its notable that BMGs have more negative ΔH_{mix} and greater δ. The zone C is representing intermediate phases that can be formed.

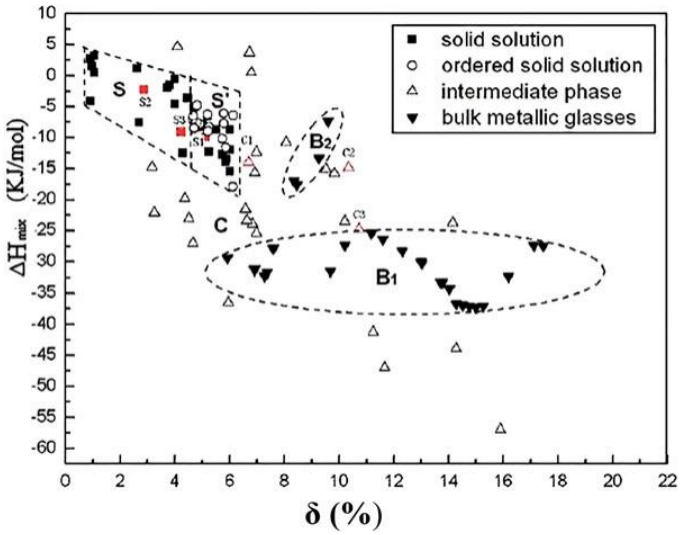

Figure 7: Phase selection diagram of HEAs and BMGs based on ΔH_{mix} and δ [50].

From equation 1, the elevated temperatures cause to increase the enthalpy of mixing (ΔS_{mix}) which considerably lower the free energy (ΔG_{mix}), and hence it will make the

solid solution further easily to form and much stable than intermetallic or other ordered phases [34]. Yang and Zhang [51] proposed the parameter Ω which combining the effect of ΔH_{mix} and ΔS_{mix} on the stability of multicomponent solid solution [51]. Ω was defined as the equation 2, where T_m is average melting temperature of the N-element alloy. Zhang at el. were reported in their research paper that that solid solution phases are highly suggested to form in HEAs when $\Omega \geq 1.1$ and $\delta \leq 6.6\%$ [52]. Also, they have reported that the solid solution formation in HEAs appeared at higher Ω and N value as shown in Figure 8.

$$\Omega = \frac{T_m \Delta S_{mix}}{|\Delta H_{mix}|} \qquad \text{Equation 2}$$

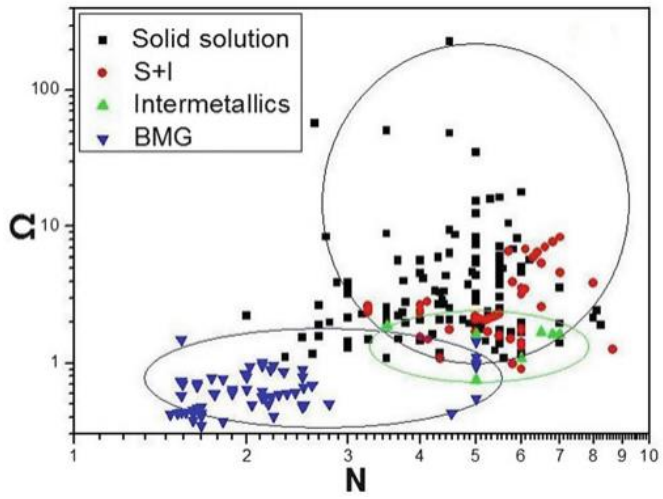

Figure 8: Phase selection diagram of HEAs and BMGs based on Ω and N [52].

The enthalpy of mixing has also reported to have an effect in determining the crystal structure in HEAs. Zhang at el provided a plot that linked the crystal structure with a function between ΔH_{mix} and δ, where from the Figure 9 the FCC-type solid solution showed to form at lower δ unlike BCC which showed to form at greater values [52]. However, the δ showed to have limited use in terms of determining the formation of FCC or BCC structured HEAs, as the FCC-type solid solution forming δ range largely overlaps with that of the BCC solid solutions.

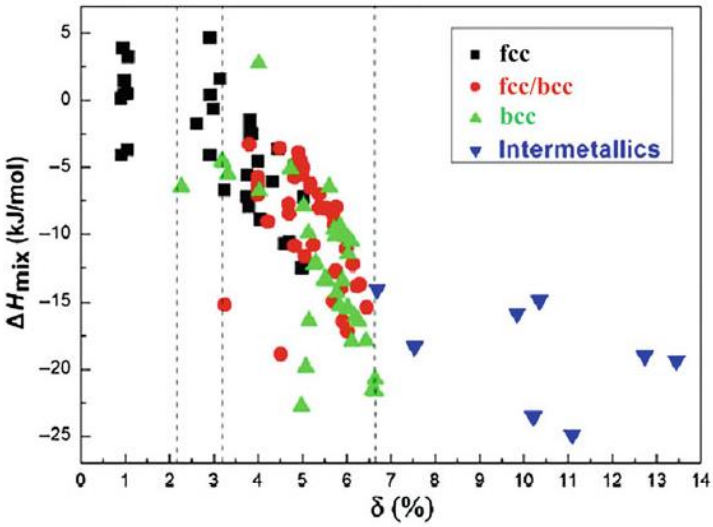

Figure 9: Dependence of crystal structures on the ΔH_{mix} and δ in various HEAs [52].

2.7 Preparation techniques

The fabrication techniques of HEAs were classified under three categories, which are: Liquid-State Route, Vapor-State Route, and Solid-State Route, as each technique have advantages and disadvantages [46]. In Figure 10 all the techniques were summarized and categorized according to the route of fabrication.

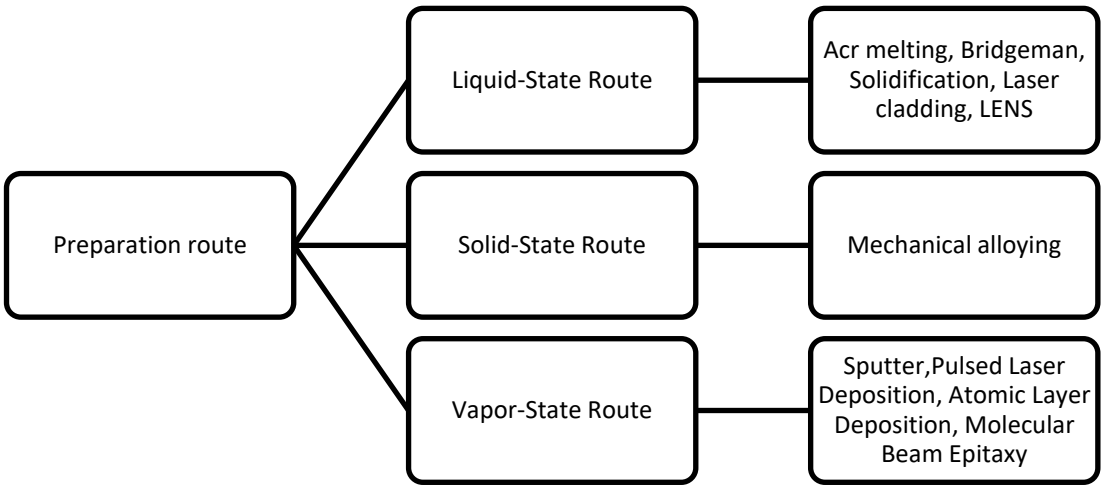

Figure 10: Preparation techniques of HEAs.

2.7.1 Liquid-State Route

The general understanding of Liquid-State Route can be explained that this method

works under the principle of melting the elements then solidify them. The arc melting method considered to be the most common method in Liquid-State Route but it has an disadvantage that the solidification process cannot be easily controlled due to the system of quick solidification. It has been reported that in as-cast state a dendritic microstructure is developed and annealing process at elevated temperatures is required to eradicate the chemical inhomogeneity [34].

2.7.2 Solid-State Route

The Solid-State Route is a method a producing HEAs from elemental powders though a technique called mechanical alloying which use a ball milling process. The powder produced in mechanical alloying is developed through a repeated cold-welding process between the powder particles. The as-milled powders is normally having a nanocrystalline structure and the annealing of as-milled powders can cause a changes in the crystal structure, where these changes depend on the alloy [34]. The long periods of milling or prolonged milling may cause to change the crystalline structure into amorphous structure by developing a sufficient free energy to the grain boundaries and defects [34]. The method of mechanical alloying has been developed by J.S. Benjamin and his colleagues [53].

2.7.3 Vapor-State Route

The Vapor-State Route is typically method for producing the thin films of HEAs and magnetron sputtering deposition is the most common method on this type of route, where it classified under physical vapor deposition techniques [34]. Molecular beam epitaxy (MBE) and atomic layer deposition (ALD) are other methods of Vapor-State Route, where they characterized in the ability of developing single-crystalline HEA films with controlling the atomic layers.

CHAPTER 3: METHODOLOGY

In this chapter the methodology of the experimental work is explained in detail, where the samples preparation, examination, and characterization will be described. In this work, HEAs of NiCrCoNb have been produced in three different compositions that contains various Al concentrations of 0%, 5%, and 10%.

3.1 Research Objective

This research aims to study the mechanical and morphological properties NiCrCoNb high entropy alloys with studying the subjected properties to the variation of aluminum concentration in the composition in three different percentages of 0%, 5% and 10%, where the computational analysis of machine learning could not provide an accurate result due to the high variation in the probabilities and the complexity of analysis.

3.2 Casting of Ingots

3.2.1 Elements collection

The ingots preparation started by collecting and weighting the elements inside the glovebox under atmosphere filled by argon gas. It worth noting that the purity of elements was 99.9% to ensure that the outcome will be produce comparable to the theoretical plan. Table 1 shows the elements concentration percentages in each composition, where the rations are varied with the change of Al and Ni concentrations, and it can be expressed in chemical formula $Ni_{55-x}Co_{30}Cr_{10}Nb_5Al_x$.

Table 1: $Ni_{55-x}Co_{30}Cr_{10}Nb_5Al_x$ HEAs Compositions and Elemental Concentrations.

HEA Composition	Ni	Co	Cr	Nb	Al
$Ni_{55}Co_{30}Cr_{10}Nb_5$	55%	30%	10%	5%	0%
$Ni_{50}Co_{30}Cr_{10}Nb_5Al_5$	50%	30%	10%	5%	5%
$Ni_{45}Co_{30}Cr_{10}Nb_5Al_{10}$	45%	30%	10%	5%	10%

3.2.2 Arc melting

After the collection process of the raw materials, the elements got melted through arc melting machine using Edmund Buhler GmbH, where this machine is working under the principle of melting the materials inside an environment filled by Argon gas and though applying electric arc struck to the elements. Arc melting technique is one of the most common techniques to prepare HEAs and it's classified under the liquid-state route [46]. Casting was carried out on a water-cooled copper crucible with a tungsten electrode upon three-time vacuum degassing and purging by Argon. It is worth noting that the first arc was initiated on a titanium ball which placed on the copper base inside the chamber in order to get rid of any remaining oxygen. Each composition melted for 5-6 times where in each attempt the electron beam hits the ingot for 25 seconds and between each attempt the sample flipped inside the machine by the arc tip in order to melt it again and ensure that all elements get fully melted. The current was initially set on 2A and increased gradually up to 4 A.

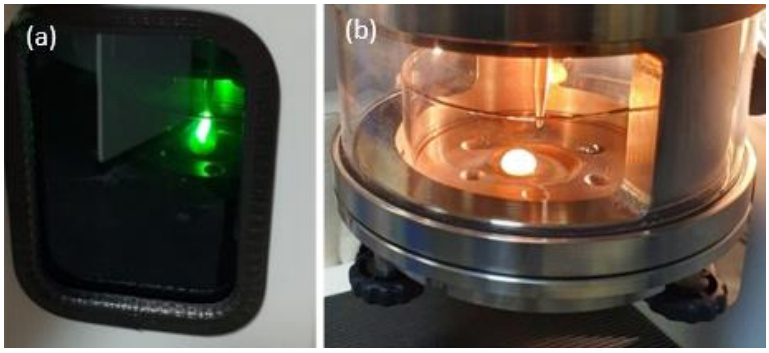

Figure 11: Ingot casting: (a) elements casting in arc melting machine, (b) the initial ingot upon finishing melting.

3.3 Metallography of the HEAs (surface preparation)

Grinding and polishing were very important in experimental work as the samples should have clear surfaces in certain processing methods (cold-rolling and fabrication of tensile samples) and characterization techniques (x-ray diffraction,

hardness test, tensile test, optical microscope, scanning electron microscope, and electron backscatter diffraction). To summarize the grinding and polishing processes, all samples were grinded first with 200, 320, 600, 800, and 1200 sandpapers respectively before reaching the polishing step with a cloth. It worth noting that alumina micro polishing solutions (0.05 and 0.1 µm) used in polishing process to provide a clear surface.

Figure 12: Metkon Forcipol 2V grinding and polishing machine.

3.4 Thermomechanical Treatments

All the arc melted ingots were annealed at 1000 ºC for 48 hours. The annealing process was carried out in a tube furnace by using GSL-1500X high temperature tube furnace (Figure 13) under mixed gas of Hydrogen and Argon (argon + 2% hydrogen). The maximum temperature inside the furnace can reach up to 1500 ºC under various gas flows. It should be noted that vacuum degassing using PFEIFFER vacuum pump and purging with mixed gas were carried out in several steps in which a vacuum pressure of 2.6×10^{-6} was reached before final purging. A zirconium plate was placed close to ingots inside the tube throughout the heat treatment to attract the any trace oxygen. A part of the produced ingots were tested later as annealed by cutting several disks (3-5 disks) from the annealed ingots through using SYJ-150 low speed diamond

saw as shown in Figure 14a.

Figure 13: Annealing process of prepared ingots at 1000 ºC for 48 hours.

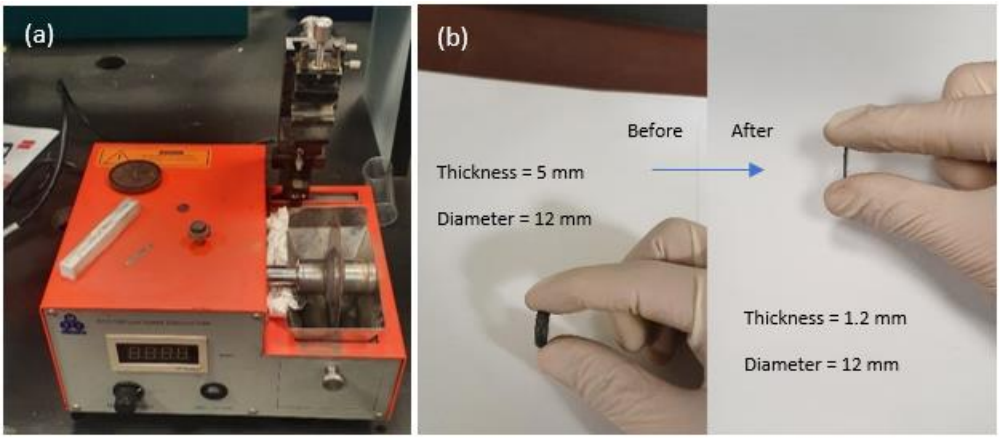

Figure 14: (a) SYJ-150 low speed diamond saw, (b) disk cutting process from annealed ingot.

Additional annealed ingots were grinded and polished to make the top and bottom surfaces flat as it went through cold rolling process after the grinding and polishing. The samples inserted in rolling machine Durston 130mm TUI-Powered Double-Sided Combination Rolling Mill (Figure 15a) where the thickness has been reduced by 62% for each ingot as presented in Figure 15b. The initial thickness of the ingot varied between 4 – 4.5 mm (depend on the manual grinding and polishing process), hence the final thickness after 62% reduction is between 1.52 – 1.71 mm. The aim of this process is to create high density of dislocations that could enable the recrystallization process after aging.

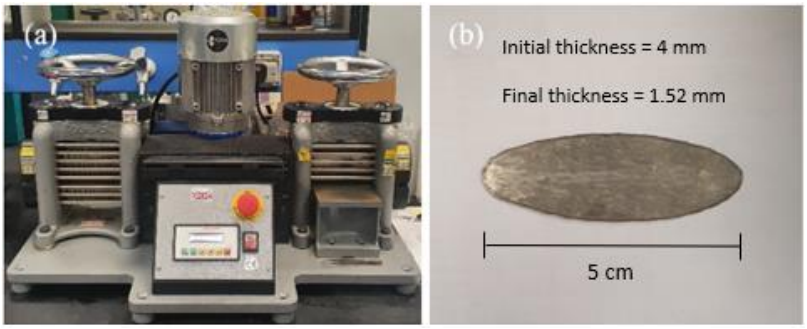

Figure 15: Cold-roll process: (a) Durston 130mm TUI-Powered Double-Sided Combination Rolling Mill, (b) ingot after cold-rolling.

The rolled samples were aged inside the furnace at several aging conditions in order to study the effect of the thermomechanical treatment on the microstructure, phase stability and mechanical properties. The aging methods which used are as following:

1. Aging at 600 ºC for 2 hours followed by air colling (CR62%+600ºC/1h).
2. Aging at 800ºC for 2 hours followed by air colling (CR62%+800ºC/1h).
3. Aging at 950ºC for 2 hours followed by air colling (CR62%+950ºC/1h).
4. Aging at 950ºC for 1 hour followed by air cooling, then 700ºC for 8 hours followed by air cooling (CR62%+950ºC/1h+700ºC/8h) (two-step treatment).

The samples were categorized based on the treatment method on the form of CR62%+aging temp/No. hour. Each sample will be later tested based on the aging process that it went through. The aging process aims to re-crystalize the sample's structure after the cold roll, but each aging process will either crystalize the structure in specific ration will not crystalize it until the sample got aged at a temperature which will cause a full crystallization.

3.5 Tensile Samples Preparation

The tensile samples were fabricated through POCKET NC CNC machine by developing a g-code in the software to define the required dimensions for the tensile samples. The dimensions of the tensile samples were around 3 mm in gauge length, 1.5 mm in width, and the thickness was varied between 0.5 to 0.68 mm as it was done

manually through grinding and polishing machine. Typically, 2 -3 tensile samples were cut from each composition and from each treatment process in order to make sure that the results accurate. Figure 16 b shows an example of the shape of tensile samples after being fabricated.

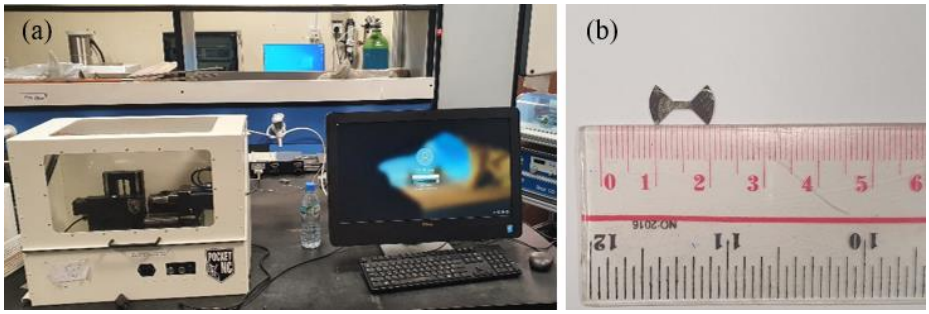

Figure 16: (a) Pocket NC CNC machine, (b) tensile sample after cut.

3.6 Morphological and Structural Characterization Techniques

Several characterization techniques were used in this work to obtain the morphological and structural information, where these techniques classified into destructive and non-destructive techniques.

3.6.1 Optical micrography

Optical images are important in characterizing the material, where it identifies the microstructure of the material and provide information about any cracks, defects, or precipitates. By using Olympus BX53M optical microscope, the microstructure images of the samples were obtained (Figure 17). It worth noting that an etching solution consisted of 10 ml CH3COOH, 5 ml HCl, and 1 g $CuSO_4$ was used in etch the surface before obtaining the microstructure images.

Figure 17: Olympus BX53M optical microscope.

3.6.2 X-ray diffraction (XRD)

X-ray diffraction is non-destructive technique which typically used to determine the phases in the crystalline materials, where it works under the principle of sending X-ray beams to the sample and then collect the signal which coming from the sample by a detector that moves in synchronized motion with the X-ray type. The XRD instrument that has been used in this work is PANalytical Empyrean diffractometer as shown in Figure 18. Each produce HEA sample was tested on XRD though a scattering angle from 10º to 90º and a step size of 0.0131º per minute. The applied voltage and tube current were 45 V and 40 mA.

Figure 18: PANalytical Empyrean diffractometer.

3.6.3 Scanning electron microscope (SEM)

The scanning electron microscopy (SEM) is an instrument that provides a magnified illustration with high resolution through using focused electron beam instead of conventional method of using the light. The interaction between the sample and electrons generates various types of signals, where the most critical signal generated from the backscattered secondary electrons (SE). Secondary electrons are very important as it provides chemical composition, morphology, and surface topography. The instrument Nova NanoSEM 450 was used in this work in imaging the fractured surfaces of tensile samples as shown in Figure 19.

Figure 19: Nova NanoSEM 450.

3.6.4 Energy dispersive spectroscopy (EDX)

Energy dispersive spectroscopy (EDX) is an extra accessory of SEM which works on exciting the inner shell electrons from the sample by hitting it with focused electron beam. EDX is normally used to identify the contributed elements and to determine the homogeneity and elemental distribution of the material.

3.6.5 Transmission electron microscopy (TEM)

The transmission electron (TEM) is another technique of microscopy forms where in works to obtain very high-resolution images for samples which less than 100 nm in thickness. Bright field and dark field are the imaging modes in TEM, where the

bright field is the most common mode. TEM is very useful in determining the structural properties such as morphology, structure, and lattice parameters in the atomic scale level. The TEM instrument that used in this work from the model TECNAI G2 TEM TF20 (Figure 20). The TEM images were obtained by placing the sample in a copper grid of 3 nm then insert it inside the vacuumed chamber which hits the sample by focused electrons beam accelerated at 200 kV.

Figure 20: TECNAI TF20 transmission electron microscope.

3.6.6 Electron backscatter diffraction (EBSD)

EBSD is an SEM-based diffraction technique which use in characterization the crystalline materials and focus on surface analysis. In EBSD, a tilted sample interacts with stationary electron beam in order to create a diffraction pattern by the diffracted electron. The diffraction pattern identifies the crystal structure and crystal orientation of the phases by providing a colored map [54]. In this study, we would like to mention the contribution of QEERI (Qatar Environment & Energy Research Institute) in providing EBSD analysis.

3.6.7 Density measurement

Density is the distribution of mass per unit area. In this work, Sartorius YDK03 density kit used to measure the produced high entropy alloys.

Figure 21: Sartorius YDK03 density kit.

3.7 Mechanical Testing

3.7.1 Hardness test

Hardness is one of the major mechanical properties that it usually should be obtained for any material that needs a mechanical understanding. It defines as the ability of the material to resistance the plastic deformation. Vickers hardness instrument of model code FM-ARS 9000 from Future-Tech company (Figure 22) was used in the experiments to obtain the hardness values of the prepared samples.

Figure 22: FM-ARS 9000 hardness testing device.

3.7.2 Tensile test

The tensile test is the most critical test to obtain the mechanical properties of a material. Though the stress-strain graph, various mechanical parameters can be

determined from this test, such as ultimate tensile strength (σ_{UTS}), Young's modulus (E), yield strength (σ_y), and ductility. The instrument used in this work was selected based on its capability to test small tensile samples. As mentioned earlier in section 3.4, the produced tensile samples in this work were relativity small compared to the conventional tensile sample. The tensile samples were tested at room temperature under quasistatic conditions at a strain rate of $10^{-3}s^{-1}$ employing a computer controlled mini tensile testing machine, which used a linear variable displacement transformer (LVDT) extensometer. The constructed system for tensile test consists of a mini tensile instrument connected into an interface device and computer where these three units are aiding in controlling the test and collect the tensile data.

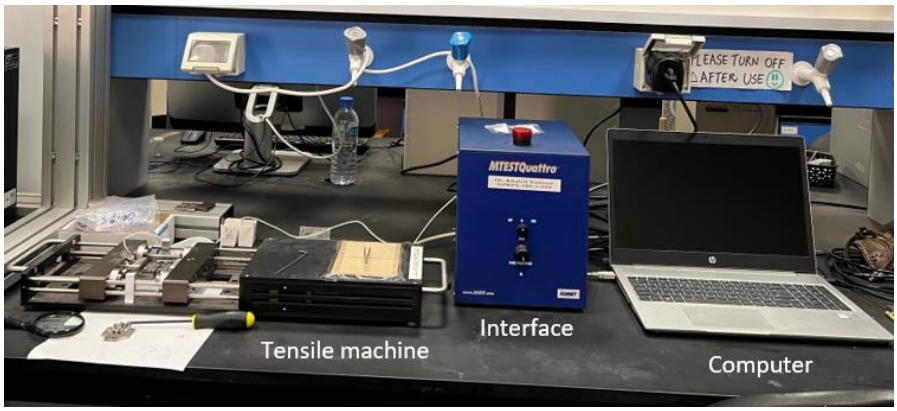

Figure 23: Tesnile machine setup.

The steps below are summarizing the process of tensile test:

1. The sample placed in the tensile machine where the grips are fixing the sample's shoulders (Figure 24 a).
2. A metallic mould place in the top of each grip as an additional support to hold the tensile specimen.
3. The grips controlled manually though the computer to make them hold the sample without any loss or extra load by monitoring the load value in the PC screen then the load and elongation are offset to zero.

4. The sample's dimensions, strain rate and other parameters are entered in the software in order to identify the test criterions.
5. The test lunched until the sample fractured then the tensile test data and graphs will be provided by the computer through the software in the form of an excel report and graph.

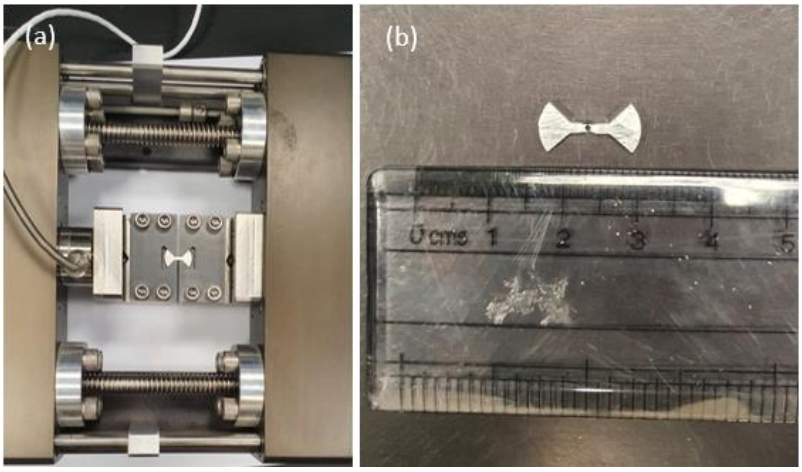

Figure 24: (a) placing of tensile sample, (b) tensile sample after fracture.

As mentioned in step 2, the load is offset manually but it will not be an accurate which cause to generate a tail in the stress-strain curve as shown in Figure 25 A. To solve this, Maplesoft® computer software was used to normalize the data and extrapolate the curves. It is worth noting that the tensile tests were performed on at least two samples for each condition to ensure numerical precision.

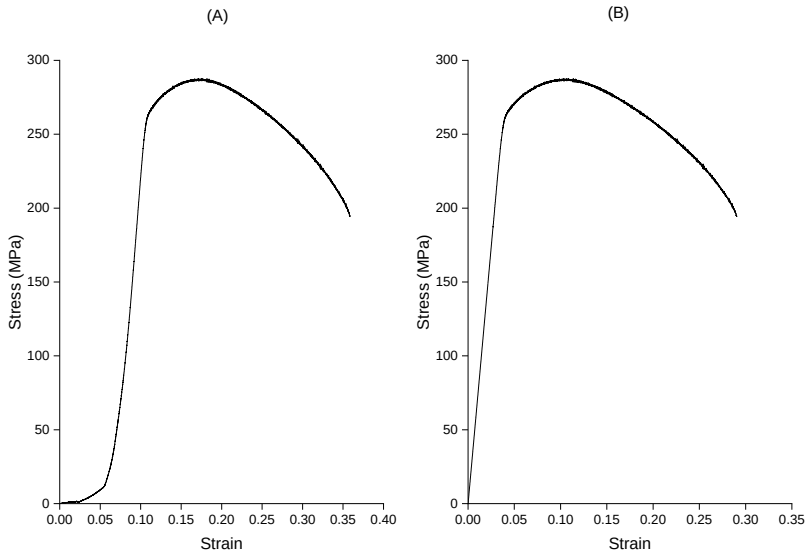

Figure 25: example of stress-strain curve adjustment. (A) initial stress-strain curve, (B) stress-strain curve after extrapolated by Maplesoft® computer software.

CHAPTER 4: RESULTS AND DISCUSSION

4.1 Morphological and Structural Properties

In this section, the morphological results by using the optical microscope, SEM, and TEM are discussed in detail based on the variation in aluminum concentration and treatment process. The effect of Al content and thermomechanical treatment on the structural properties and phase analysis of the HEAs are described using XRD, SEM, TEM, and EBSD analyses. These analyses should help us understand the mechanical behavior of the processed HEAs.

4.1.1 Morphological and Structural Properties of $Ni_{55}Co_{30}Cr_{10}Nb_5$ (0% Al)

The microstructures of $Ni_{55}Co_{30}Cr_{10}Nb_5$ processed at different processing conditions are shown in Figure 26. The annealed ingot showed a typical crystallized structure that has relativity large grains. It is also observed that most of the grains contains annealing twins with no presence of second phase precipitation at the grain boundaries. Figures 26 (b) and (c) shows the optical micrographs of the $Ni_{55}Co_{30}Cr_{10}Nb_5$ alloy after cold rolling of the annealed ingot with 62% reduction and aging at 600ºC and 800ºC, respectively. It can be seen that all the grains are elongated in the rolling direction with high density of shear bands contained inside the elongated grains. It is worth noting that the aging process at 600ºC and 800ºC for 1 hours did not case recrystallization changes in the deformed structure. Figure 26 (d) and (e) shows the optical micrographs of CR62%+950ºC/1h and the CR62%+950ºC/1h+700ºC/8h, where structural crystallization occurs for both ingots with notable annealing twins in the samples. microstructure with notable smaller grains than the annealed ingot.

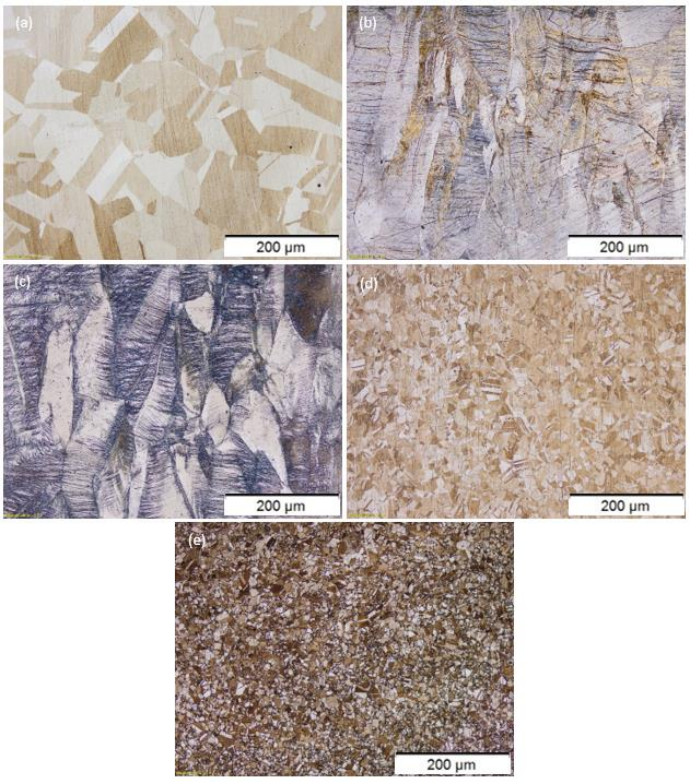

Figure 26: Microstructure images of $Ni_{55}Co_{30}Cr_{10}Nb_5$ from optical microscope at all treatment mehtods: (a) as-annealed, (b) CR62%+600ºC/1h, (c) CR62%+800ºC/1h, (d) CR62%+950ºC/1h (e) CR62%+950ºC/1h+700ºC/8h.

By using ImageJ® computer software, the averages of grain size were calculated for the crystalized samples as summarized in Figure 27. The obtained grain sizes showed a significant reduction after each aging process, which could affect the mechanical behavior of these aged samples. The obtained grain sizes where 229, 62.4 and 33.7 µm for annealed, CR62%+950ºC/1h and CR62%+950ºC/1h+700ºC/8h, respectively. The two-step heat treatment causes to reduce the grain size to 33.7 um which recorded as the smallest grain size upon all treatment conditions.

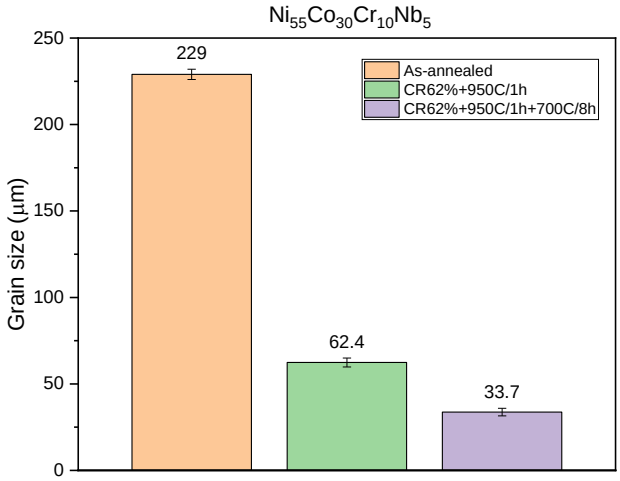

Figure 27: The average grain sizes of $Ni_{55}Co_{30}Cr_{10}Nb_5$ at different thermo-mechanical treatments.

Figure 28 displays the XRD patterns of the produced $Ni_{55}Co_{30}Cr_{10}Nb_5$ alloy at all processing conditions. All produced samples with varied processing methods showed that formation of an FCC as main phase with XRD peaks at 44º, 51.1º, 75.3º, 91.3º and 96.8º, which correspond to (111), (200), (220), (311), and (222) atomic planes respectively. Whereas the second phase reveals at 41.5º, 47.2º, and 82.4º corresponding to (002), (101), and (103) planes respectively manifesting hexagonal closed packed structure (HCP). In addition, a second FCC phase observed on XRD at closed peaks to the main FCC phase. From the intensity of peaks, it's clear that FCC phase is the dominated phase at all processing conditions of $Ni_{55}Co_{30}Cr_{10}Nb_5$ HEA. The as-annealed, cold-rolled 800 ºC aged, and cold-rolled 950 ºC aged samples displayed a significant preferred grain-orientation at (111) plane for the FCC phase, unlike cold-rolled 600 ºC aged ingot which showed preferred grain-orientation at (220) plane for the FCC phase. From the obtained results, the material showed to be dominated by FCC crystal structure at all processing methods where the only difference found in preferable phase orientation at cold-rolled 600 ºC aged ingot. It worth noting that the indication of

FCC crystal structure from XRD gave a prediction of a good ductility for the prepared samples, whereas has been discussed earlier in Chapter 2 the FCC crystal structure is typically provide a ductility between 20% - 60%.

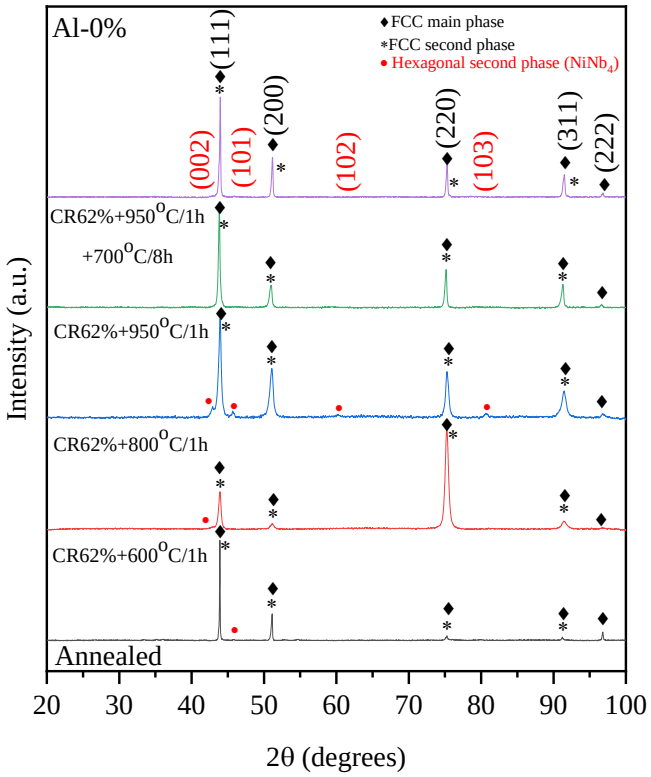

Figure 28: XRD results of $Ni_{55}Co_{30}Cr_{10}Nb_5$ at all processing methods.

4.1.2 Morphological and Structural Properties of $Ni_{50}Co_{30}Cr_{10}Nb_5Al_5$ (5% Al)

The morphological results of $Ni_{50}Co_{30}Cr_{10}Nb_5Al_5$ showed a similar behavior to $Ni_{55}Co_{30}Cr_{10}Nb_5$ where the recrystallization occurred initially at 950 ºC after the cold rolling. Figure 29 shows the optical micrographs images of $Ni_{50}Co_{30}Cr_{10}Nb_5Al_5$ at all processing conditions at the magnification of 100X. Figure 29A displays the microstructure of annealed ingot, where the image showed large grains in addition of annealing twins. Figures 29 B and C show the optical micrographs of cold-rolled aged ingots at 600 ºC and 800 ºC, where deformed structure appeared with elongated grains and shear bands with high density of dislocations, which confirmed that the aging temperatures at 600 ºC and 800 ºC are not sufficient to re-crystalize the deformed

structures.

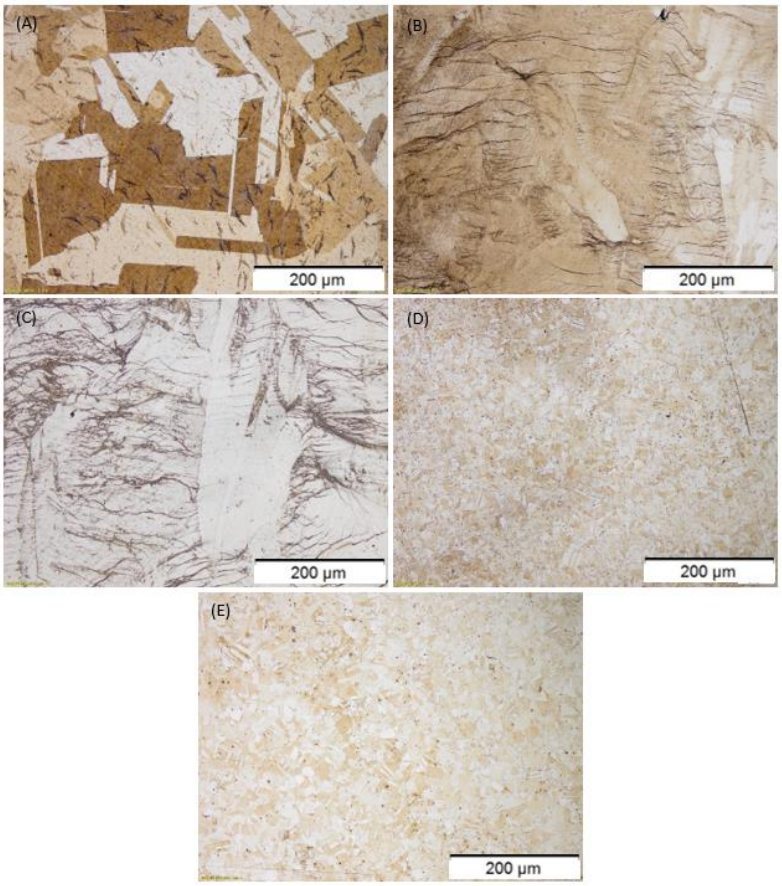

Figure 29: Microstructure images of $Ni_{50}Co_{30}Cr_{10}Nb_5Al_5$ from optical microscope at all treatment methods: (a) as-annealed, (b) CR62%+600ºC/1h, (c) CR62%+800ºC/1h, (d) CR62%+950ºC/1h (e) CR62%+950ºC/1h+700ºC/8h.

The optical micrographs of CR62%+950ºC/1h and CR62%+950ºC/1h+700ºC/8h ingots are shown in Figure 29 D and E. Both samples displayed recrystallized structures, in addition of twinning defects and precipitates with notable variation in grain size between annealed and recrystallized ingots as summarized in Figure 30. It is worth noting that the recrystallization occurred at condition CR62%+950ºC/1h similar to $Ni_{55}Co_{30}Cr_{10}Nb_5$ HEA. The grain size calculation showed high reduction from 223.5 to 50.8 µm after aging process at 950ºC, where the obtained grain sizes are 223.5 µm, 48.2µm and 50.8µm for annealed, CR62%+950ºC/1h and CR62%+950ºC/1h+700ºC/8h, respectively. It's worth to mention that the double heat

treatment method did not affect the grain size as the grain size kept almost the same as 950 ºC aged sample.

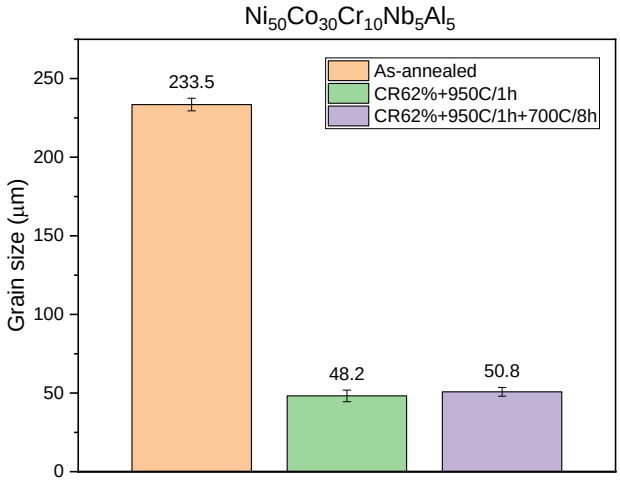

Figure 30: Grain sizes of $Ni_{50}Co_{30}Cr_{10}Nb_5Al_5$ at all treatment methods with exclude uncrystilized structures from grain size evaluation.

Figure 31 shows the XRD results of $Ni_{50}Co_{30}Cr_{10}Nb_5Al_5$ at different heat treatments. The XD peaks indicates the formation of FCC solid solution with another FCC second phase at (111), (200), (220), (311) and (222) atomic planes. Also, HCP second phase observed at XD pecks (002), (101), (102) and (103). The samples which cold-rolled and aged at 600ºC and 800ºC were showed to have a preferred FCC phase orientation at (111) plane, unlike as-annealed and cold-rolled 950ºC aged samples which showed to have a preferred FCC phase orientation at (200). The double heat-treated sample showed to have a preferred phase orientation at (111) like the 600ºC and 800ºC aged samples.

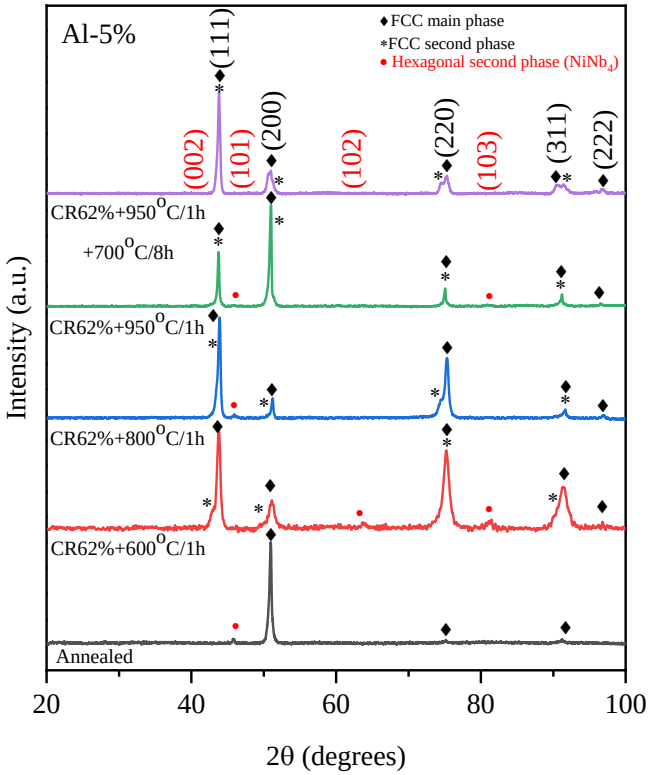

Figure 31: XRD results of $Ni_{50}Co_{30}Cr_{10}Nb_5Al_5$ at all processing methods.

The samples for TEM and EBSD were prepared away from the grain boundaries using the site-specific lift out technique focused ion beam (FIB). A lift-out was initially prepared with the help of OmniProbe micro-manipulator in FIB and this lift-out is subsequently thinned to appropriate dimensions for TEM and EBSD, in multiple steps by progressively reducing the voltage and/or current of the Ga ion beam in the dual-beam FIB. Figure 32 presents the atomic resolution high angle annular dark field (HAADF) images from transmission electron microscope (TEM) and corresponding elemental mapping by EDS of the NiCrCoNbAl HEA processed at CR62%+950ºC/1h+700ºC/8h. On every EDS map of a particular element, the brightness of an individual spot rises with the number of atoms and thus represents the local density of the element. From Figure 31, a random density variation was noticed between all contributed elements, where Ni, Al, and Nb showed related degree of

homogeneity and Co and Cr showed another similar degree of homogeneity. These results showed a chemical ordering between NiAlNb and CrCo to form a single-phase FCC, which can be linked to the superior strength and ductility of this HEA. The local chemical ordering and chemical short-range order (CSRO) was reported recently to be one of the reasons for the superior mechanical properties in HEAs that originate from possible local chemical fluctuations and distorted lattices [55]–[57] which inherently related with the thermodynamics that controls solid solution formation in HEAs [58], [59]. Liu et al. studied the CSRO in $Fe_{50}Mn_{30}Co_{10}Cr_{10}$ HEA, and mentioned that the CSRO was found after recrystallization annealing [60]. In our study, the chemical range order was found after recrystallization the structure at double heat treatment CR62%+950ºC/1h+700ºC/8h.

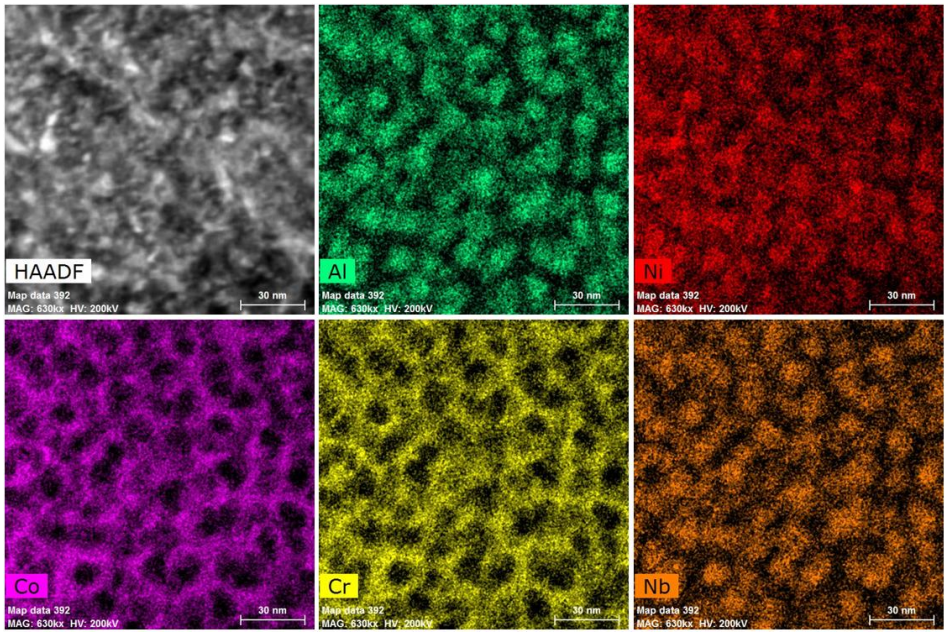

Figure 32: TEM and EDS mapping for $Ni_{50}Co_{30}Cr_{10}Nb_5Al_5$ HEA processed at 950ºC+700ºC showing CSRO between Cr-Co and Al-Ni-Nb atomic pairs.

Similar chemical orderings have been reported in several studies, where Gao et al. had reported the chemical ordering between Al-Ni, Fe-Cr, and Co-Cr atomic pairs in the $Al_{1.3}$CoCrCuFeNi HEA through ab initio molecular dynamics simulations (AIMD)

[61]. Also, a similar finding of CSRO was reported by Singh at el. for the HEA AlCoCrFeNi [62]. In addition, CSRO was reported to enhance the strength and ductility of CoCrNi MEAs by obstructing the dislocation motion during the deformation [63], [64]. Moreover, three short-range chemical orderings were found in CoCrFeMnNi HEAs, which are Mn-Ni, Cr-Cr, and Co-Fe, and these CSROs indicated a possible enhancement in ductility by adjusting the dislocations distribution and size as it preferring to originate in the Cr-Cr region [65], [66]. These results showed a similar CSRO to our findings since the TEM and EDS exhibited a chemical ordering between Cr-Co and Al-Ni-Nb atomic pairs.

Figure 33 shows the EDS mapping of the $Ni_{50}Co_{30}Cr_{10}Nb_5Al_5$ sample with the two-step treatment. It can be seen that the elements are uniformly distributed through the microstructure with the presence of Nb-rich-phase precipitation at the grain boundaries. It can be seen that the size of the second phase precipitation is much smaller than the precipitates observed after aging at 950ºC for 1 hour (see Figure 29).

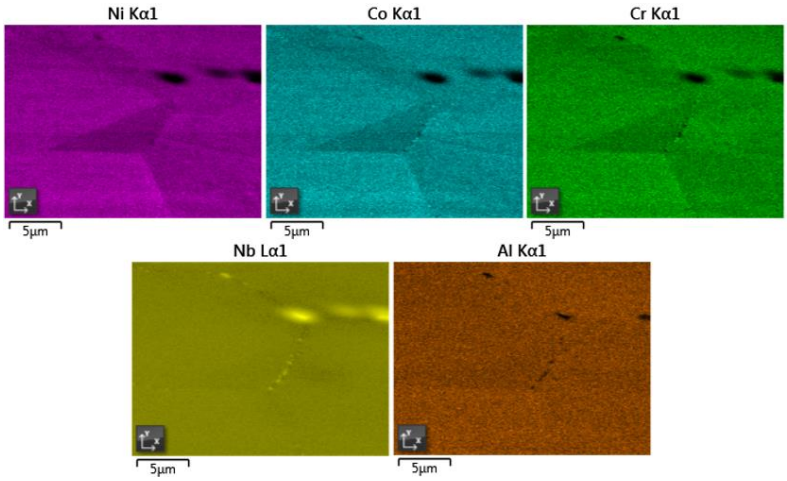

Figure 33: Elemental mapping showing the distribution of the contributed elements for the sample CR62%+950ºC/1h+700ºC/8h.

Figure 34 shows the inverse pole figures (IPF) and phase mapping of the $Ni_{50}Co_{30}Cr_{10}Nb_5Al_5$ sample with the two-step treatment. The IPF and phase mapping

showed a preferred FCC phase orientation at (001), (101) and (111) which confirm the XRD result of the CR62%+950ºC/1h+700ºC/8h ingot.

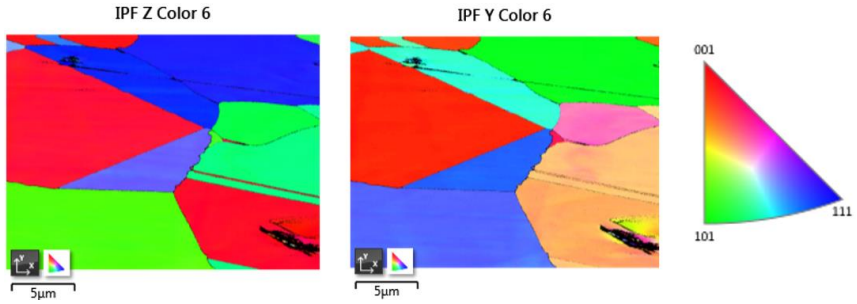

Figure 34: EBSD mapping shows a random orientation of the grains in $Ni_{50}Co_{30}Cr_{10}Nb_5Al_5$ HEA processed at CR62%+950ºC/1h+700ºC/8h.

A line scan has been done for the observed nanoprecipitates in the processed sample at 950ºC+700ºC. The results (Figure 35) confirmed that all contributed elements decreased within the precipitates range except niobium which showed to increase to its highest level. This result showed that the precipitates in the sample are mainly a niobium-rich phase. Yan et al [67] reported that both the CSRO and precipitates have been classified as one of the main strengthening mechanisms for HEAs.

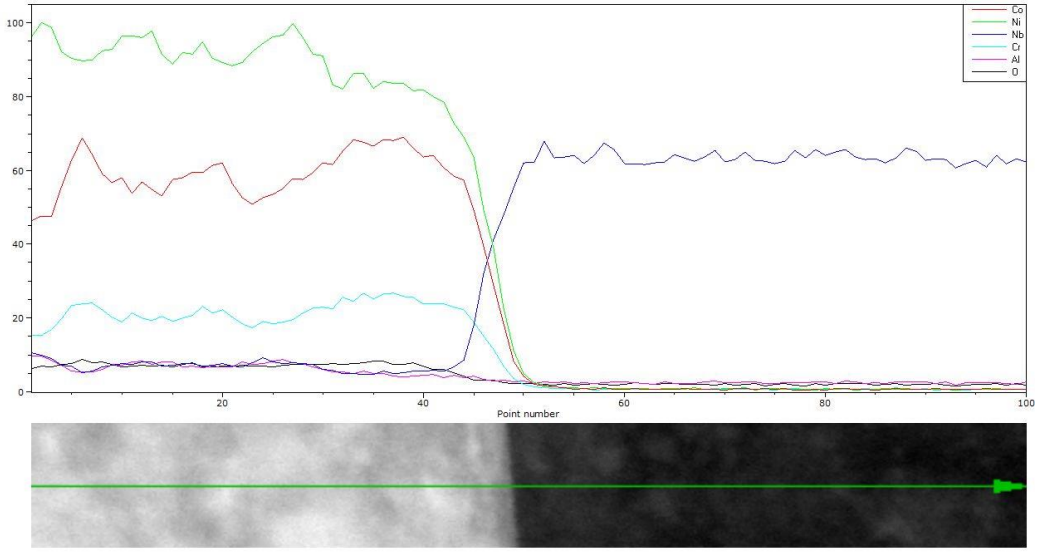

Figure 35: High resolution TEM line scan in $Ni_{50}Co_{30}Cr_{10}Nb_5Al_5$ HEA processed at CR62%+950ºC/1h+700ºC/8h.

4.1.3 Morphological and Structural Properties of $Ni_{45}Co_{30}Cr_{10}Nb_5Al_{10}$ (10% Al)

The morphological results of $Ni_{45}Co_{30}Cr_{10}Nb_5Al_{10}$ were different than the rest of the compositions. In annealed ingot, the optical micrograph image showed a typical dendritic structure as shown in Figure 36A, where the dendritic structure occurs when the main growth direction is against the heat flow direction during the solidification [68]. The grain size was calculated for as-annealed ingot and was found to be 349 µm.

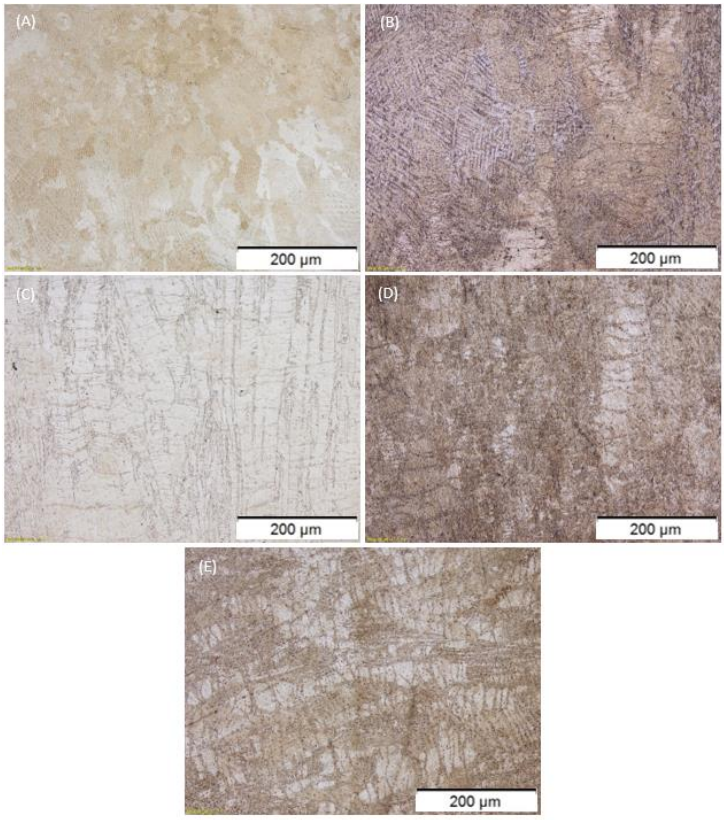

Figure 36: Microstructure images of $Ni_{45}Co_{30}Cr_{10}Nb_5Al_{10}$ from optical microscope at all treatment methods: (a) as-annealed, (b) CR62%+600ºC/1h, (c) CR62%+800ºC/1h, (d) CR62%+950ºC/1h (e) CR62%+950ºC/1h+700ºC/8h.

The cold-rolling and aging processing at temperatures 600ºC, 800ºC, 950ºC and two-step treatment was not sufficient to re-crystallize the material structure and as shown in Figures 36 B, C, D and E. From these results, it is notable that the increment of the Al ratio to 10% makes the re-crystallization process requires a higher temperature.

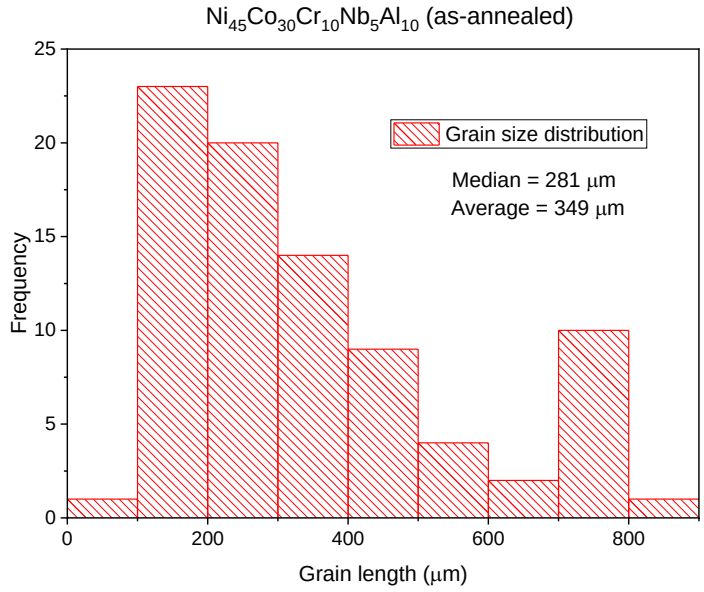

Figure 37: Calculation of grain size for $Ni_{45}Co_{30}Cr_{10}Nb_5Al_{10}$ as-annealed.

The analyzed XRD results of $Ni_{45}Co_{30}Cr_{10}Nb_5Al_{10}$ (Figure 38) showed the existence of the same phases in $Ni_{55}Co_{30}Cr_{10}Nb_5Al_0$ and $Ni_{50}Co_{30}Cr_{10}Nb_5Al_5$ of FCC and HCP. The dominated phase observed to be FCC with variance in preferable orientation at each treatment condition. The annealed and CR62%+600ºC/1h showed that the FCC phase preferred the orientation at (200) atomic plane. The CR62%+800ºC/1h sample showed exceptional FCC phase orientation at (220) and (311) atomic planes. The CR62%+950ºC/2h sample demonstrated main FCC phase orientation at (111) and (200) atomic planes. The two-step treatment shifts the favored orientation of FCC phase to (111) and (220). In general, the dominated phase in the $Ni_{45}Co_{30}Cr_{10}Nb_5Al_{10}$ alloy stayed as FCC at all processing conditions but the phases orientations were varied between each processing condition. HCP second phase observed for the $Ni_{45}Co_{30}Cr_{10}Nb_5Al_{10}$ HEA at all treatment conditions at (002), (101), (102), and (103) atomic planes, where the HCP second phase indicated to be as precipitation.

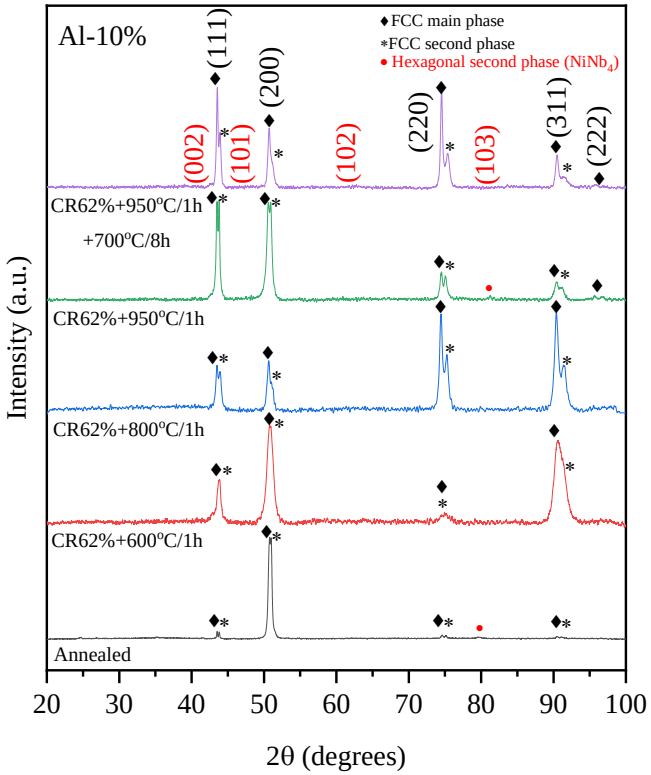

Figure 38: XRD results of $Ni_{45}Co_{30}Cr_{10}Nb_5Al_{10}$ at all processing methods.

4.1.4 Effect of Al Concentration on the Morphological and Structural Properties

The morphological results of the produced HEAs along all processing conditions showed some similarities and differences in three main aspects which are: the grain size, phase type, and recrystallization temperature. The annealed HEAs of 0 and 5% Al concentrations showed typical crystal structure with twinning defect, but the 10% Al showed a dendritic phase unlike the other compositions. After cold rolling, the microstructures of all HEAs were observed and found that the aging temperature at 950ºC for two hours is sufficient to cause a recrystallization for 0%Al and 5%Al HEAs only, but it was not adequate to recrystallize the structure of 10% Al HEA. Also, the two-step treatment could form structure of 0% and 5% HEAs, and it could not recrystallize the structure of 10% Al HEA. From these results, we observed that the increment in Al concentration to 10% increase the required aging temperature for recrystallization as none of the applied processing conditions could cause

recrystallization to $Ni_{45}Co_{30}Cr_{10}Nb_5Al_{10}$ structure after cold rolling.

To evaluate additional structural marks for the produced HEAs, the density had calculated for each composition as shown in the Figure 39, where the obtained results showed a clear inverse relation between the Al concentration and density, hence that each 5% increment in Al caused a decrement of 0.3 g/cm^3 in the alloy's density.

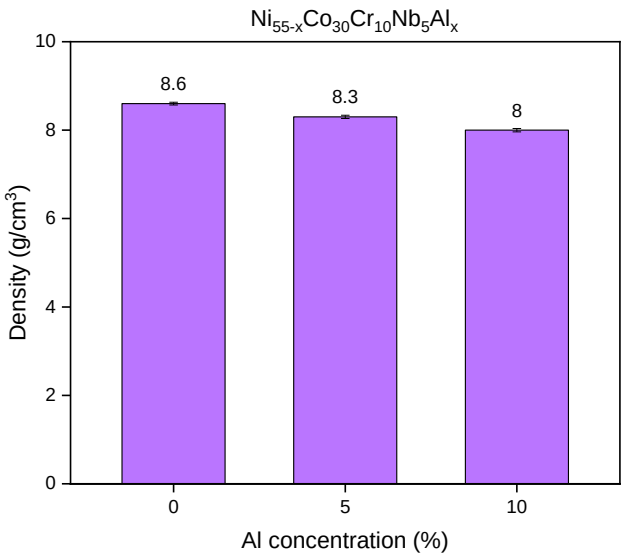

Figure 39: Density of produced HEAs versus the Al concentration at CR62%+950ºC/1h+700ºC/8h.

The structural results of the produced HEAs along all processing conditions proved that the variation in Al concentration at 0, 5, and 10% did not improve in structure, where the FCC phase was dominating the HEAs structure at each time. However, the only point that has been noticed is the alternation in atomic planes orientation between each processing method and at each Al concentration. It has been noted that annealed ingots at 5 and 10% Al preferred to orient on plane (200), unlike 0% Al which showed a preferable FCC phase orientation on the (111) atomic plane. So, the final note is that adding Al to NiCoCrNb HEA shifts the phases orientation from (111) to (200).

4.2 Mechanical Properties

In this section, the mechanical properties obtained from hardness and tensile

tests are discussed in detail based on the Al content and treatment process. Also, the effect of thermomechanical treatment is linked with the mechanical properties variation in order to select the most optimum treatment condition for the produced HEAs. The mechanical properties that determined are: yield strength (σ_y), ultimate tensile stress (σ_{UTS}), uniform strain (ε_u), strain hardening exponent (n), ductility, and hardness.

4.2.1 Mechanical Properties of $Ni_{55}Co_{30}Cr_{10}Nb_5$ (0% Al)

Figure 40 shows the true stress versus accurate strain curves for annealed, CR62%+600ºC/1h, CR62%+800ºC/1h, CR62%+950ºC/1h and CR62%+950ºC/1h+ 700ºC/8h. By starting with the annealed sample, a high ductility of 75% was observed with an ultimate tensile strength of 967 MPa and yield strength of 291 MPa as summarized in Figures 41, 44 and 43. The Vickers hardness test of annealed ingot showed a result of 2.4 GPa which was found to be the lowest value upon all treatment conditions for $Ni_{55}Co_{30}Cr_{10}Nb_5Al_0$ HEA.

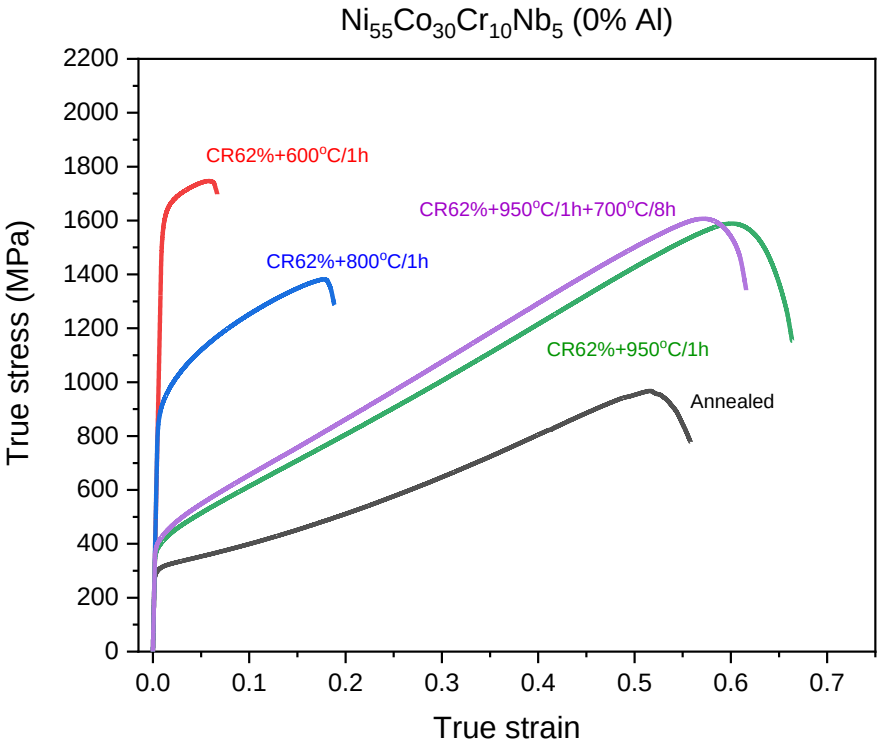

Figure 40: True stress-strain curves of $Ni_{55}Co_{30}Cr_{10}Nb_5$ at all processing methods.

The observed ductility of CR62%+600ºC/1h sample was recorded as 6.9% which then indicated to be the lowest ductility. The observed yield strength and UTS recorded as 1589 and 1747 MPa, respectively, where the values are relatively closed to each other due to the occurrence of the fracture after short range of the elastic and plastic regions. The hardness gave an earlier indication about the low ductility as its measured as 4.6 GPa which is the highest value upon all prepared samples as brief in Figure 41.

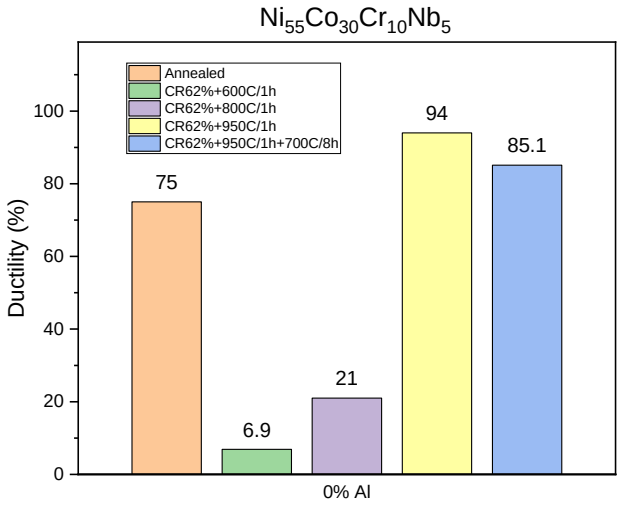

Figure 41: Ductility results of $Ni_{55}Co_{30}Cr_{10}Nb_5$ at all processing methods.

For the sample aged at 800ºC, the ductility has been increased to reach 21% with 873 MPa yield strength and 1382 MPa ultimate tensile strength. The measured hardness found decreased to 3.3 GPa after 800ºC aging treatment, and this decrement played a role in increase the ductility of the sample.

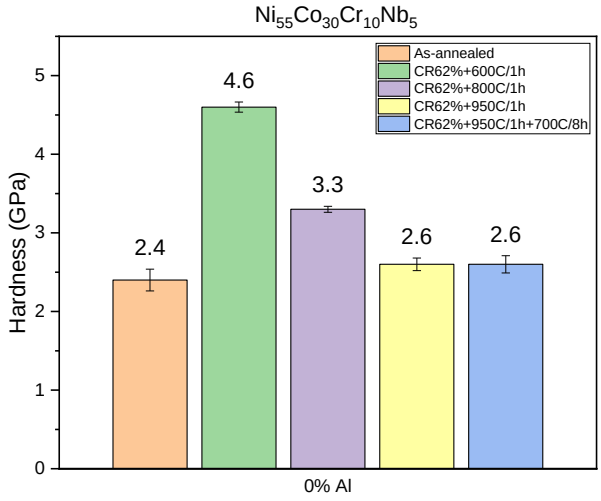

Figure 42: Hardness of $Ni_{55}Co_{30}Cr_{10}Nb_5$ at all processing methods.

The CR62%+950ºC/1h ingot showed an excellent enhancement in the mechanical properties where the yield strength and UTS recorded as 385 and 1588 MPa

respectively with a hardness of 2.6 GPa and ductility of 94%, which is the highest observed value of ductility upon all treatment methods. The recrystallization of the ingot's structure played role in redistribute the precipitates and defects. Also, the significant decrement in grain size helped in improve the mechanical properties in general, as the inverse relation between grain size and mechanical properties [69].

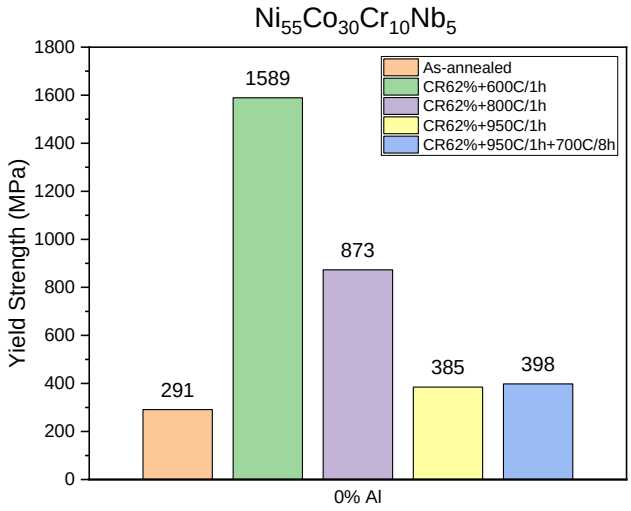

Figure 43: Yeild strength of $Ni_{55}Co_{30}Cr_{10}Nb_5$ at all processing methods.

The sample CR62%+950ºC/1h+700ºC/8h exhibits almost the same mechanical properties of CR62%+950ºC/1h with slight improvement. By starting with stress-strain curve, the sample showed yield strength and UTS of 398 and 1606 MPa respectively with total fracture elongation of 85%. The hardness did not change and stayed at 2.6 GPa and the uniform strain was obtained as 57.2%, which is close to the CR62%+950ºC/2h sample, as well as the strain hardening which has been obtain as 0.39. From the results, the double heat treatment did not make any significant changes for $Ni_{55}Co_{30}Cr_{10}Nb_5$ HEA from structural and mechanical respective. Hence, The CR62%+950ºC/2h can be selected as the most suitable treatment method for $Ni_{55}Co_{30}Cr_{10}Nb_5$ HEA in respective of saving time and energy as it provides excellent properties of high strength and ductility.

From the analyzed mechanical properties and by compare them to the heat treatment methods, it's clear that the effect of aging temperature showed an inverse relationship with the yield strength and hardness except the CR62%+950ºC/1h+700ºC/8h which showed a slight increment in yield strength. On the other hand, a proportional relationship appeared between the aging temperature and ductility, uniform strain, and strain hardening exponent at all treatment conditions except the CR62%+950ºC/1h+700ºC/8h which showed a slight decrement.

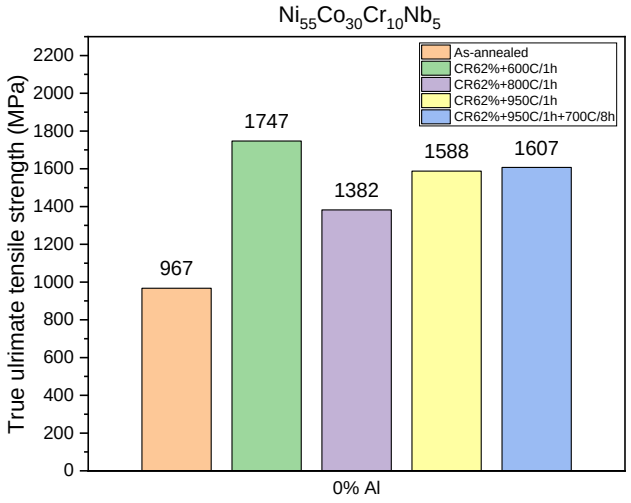

Figure 44: True ultimate tensile strength of $Ni_{55}Co_{30}Cr_{10}Nb_5$ at all processing methods.

The true uniform strain observed to be the greatest on CR62%+950ºC/1h and CR62%+950ºC/1h+700ºC/8h samples as 77% and 72.7% respectively, where both samples uniformly deformed on plastic part for a high range. Figure 45 is summarizing the true uniform strain values for composition $Ni_{55}Co_{30}Cr_{10}Nb_5Al_0$ at all processing methods.

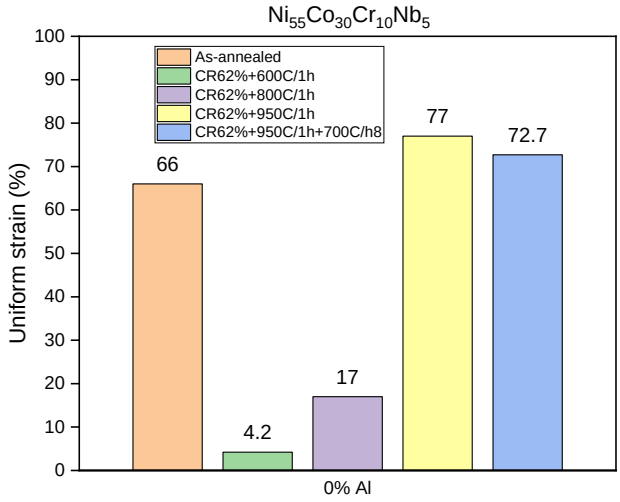

Figure 45: Unifrom strain of $Ni_{55}Co_{30}Cr_{10}Nb_5$ at all processing methods.

The strain hardening exponent has been calculated and found to be the highest at CR62%+950ºC/1h and CR62%+950ºC/1h+700ºC/8h samples as 0.4 and 0.39 respectively, where both ingots showed good formability as the uniform deformation happened at long range in the plastic part Figure 46.

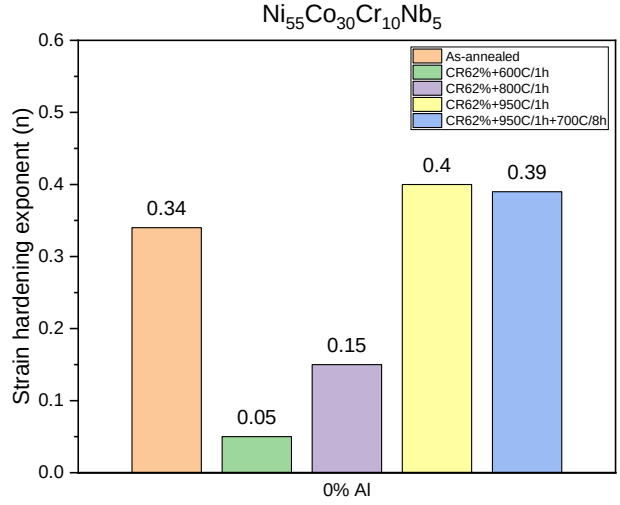

Figure 46: Strain hardening exponents of $Ni_{55}Co_{30}Cr_{10}Nb_5$ at all processing methods.

It is obvious from the analyzed mechanical properties of the HEA with 0%Al that the 950ºC showed almost the best combination of strength and ductility. These

extraordinarily mechanical properties could in advanced applications, especially the true UTS, which exceed more than 1588 MPa with ductility of 94%.

4.2.2 Mechanical Properties of $Ni_{50}Co_{30}Cr_{10}Nb_5Al_5$ (5% Al)

Figure 47 shows the true stress-strain curves for the $Ni_{50}Co_{30}Cr_{10}Nb_5Al_5$ HEAs processed at different thermomechanical treatments. All the processing methods produced a yield strength higher than 800 MPa which gave a high elastic range of for all prepared ingots at all treatment conditions.

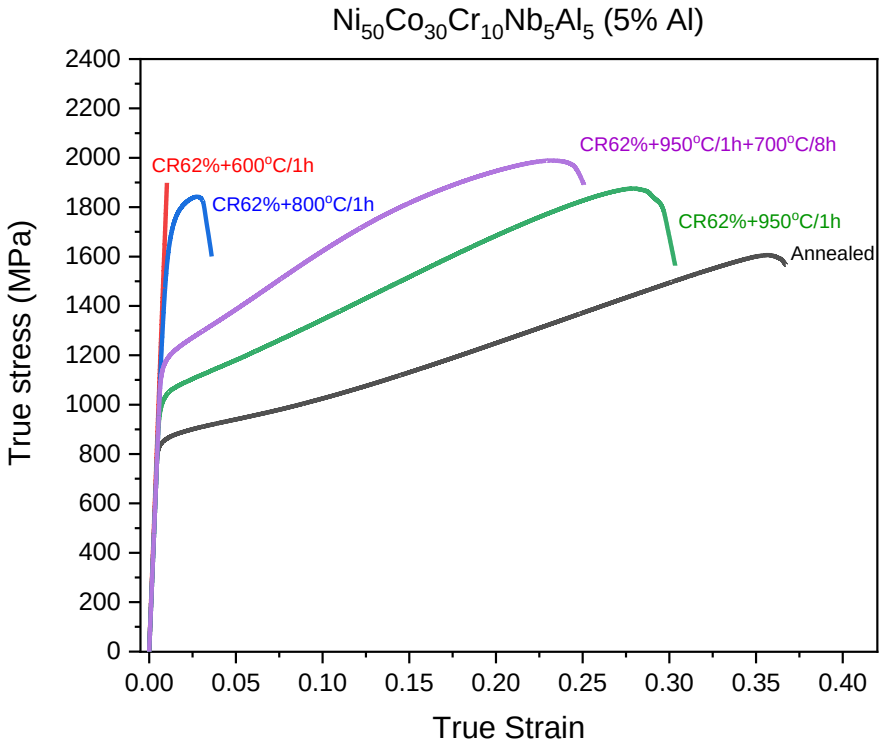

Figure 47: True stress-strain curves of $Ni_{50}Co_{30}Cr_{10}Nb_5Al_5$ at all processing methods.

The annealed sample gave an excellent ductility of 44% beside a yield strength and ultimate tensile strength of 840 and 1606 MPa, respectively. The aging process at 600ºC improved the yield strength of the material to 1812 MPa and the ultimate tensile strength to 1898 MPa, but it had reduced the ductility to 1% where the sample fractured at almost the yield point.

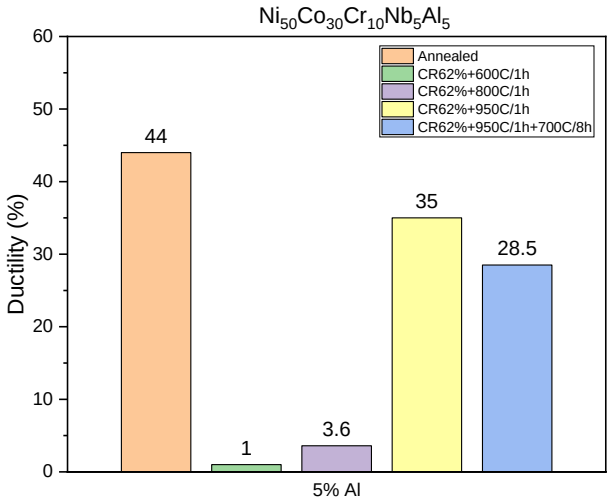

Figure 48: Ductility results of $Ni_{50}Co_{30}Cr_{10}Nb_5Al_5$ at all processing methods.

The HEA aged at 800ºC showed a significant improvement in the ductility above that of the sample aged at 600ºC. The ductility has been improved to 3.6% which is higher than CR62%+600ºC/1h sample as shown in Figure 48. The low ductility of CR62%+600ºC/1h and CR62%+800ºC/1h samples was an outcome of the uncrystallized structures that has absence of grains boundaries and unclear grain which not providing a conventional fracture mechanism. However, the yield strength and ultimate tensile strength were unprecedented and exceptional with values of 1650 and 1842 MPa respectively. The 950ºC aging treatment showed an improvement in ductility to 35% and in yield strength to 1014 MPa. The observed ultimate tensile strength of CR62%+950ºC/1h sample noted to reach 1875 MPa. The CR62%+950ºC/1h+700ºC/8h sample showed exceptional mechanical properties with yield strength of 1170 MPa, 28.5% of ductility and 1988 MPa of UTS. The two-step treatment provides the highest ultimate tensile strength with excellent ductility and yield strength which made the alloy hard and ductile at same moment.

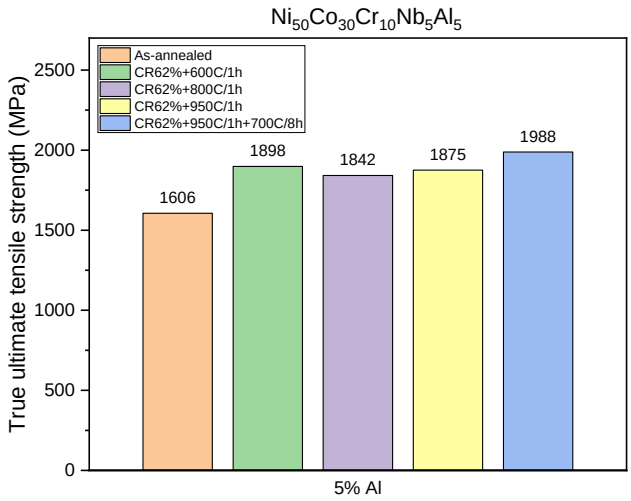

Figure 49: True ultimate tensile stregnth values of $Ni_{50}Co_{30}Cr_{10}Nb_5Al_5$ at all processing methods.

The yield strength values showed an inverse relation with the aging temperature whereas the aging temperature increase the yield strength decrease as shown in Figure 50. But the two-step treatment exhibited different behaviour where the yield strength got increase again to 1170 MPa after being reduced to 1014 MPa. This could be explained as the precipitates were distributed in an effective way to cause increment in the strength of alloy. The interesting observation that the yield point after all aging conditions did not decrease in less than 1000 MPa and that gave the alloys high elastic range.

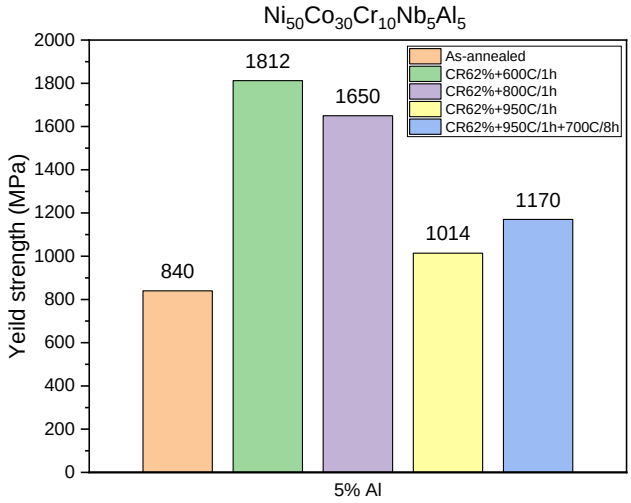

Figure 50: Yeild strength of $Ni_{50}Co_{30}Cr_{10}Nb_5Al_5$ at all processing methods.

The hardness values presented to be around 4.3 to 4.4 at most treatment conditions except at CR62%+600ºC/1h aging and CR62%+950ºC/1h+700ºC/8h samples which presented an increment in hardness to 6.8 and 5 GPa respectively as expressed in Figure 51.

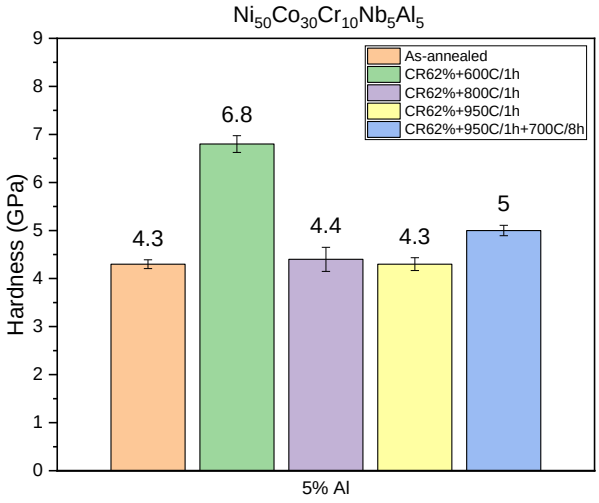

Figure 51: Hardness of $Ni_{50}Co_{30}Cr_{10}Nb_5Al_5$ at all processing methods.

The strain hardening exponent of CR62%+600ºC/1h did not calculated as the tensile sample fractured after very short range of yield point, which means that the specimen

gave very low formability. Figure 52 briefing the strain hardening exponents of $Ni_{50}Co_{30}Cr_{10}Nb_5Al_5$ at all treatment conditions where the annealed, CR62%+950ºC/1h and CR62%+950ºC/1h+700ºC/8h specimens appeared a value of 0.2. The lowest strain hardening exponent value was observed on the CR62%+800ºC/1h aged sample due to its low formability.

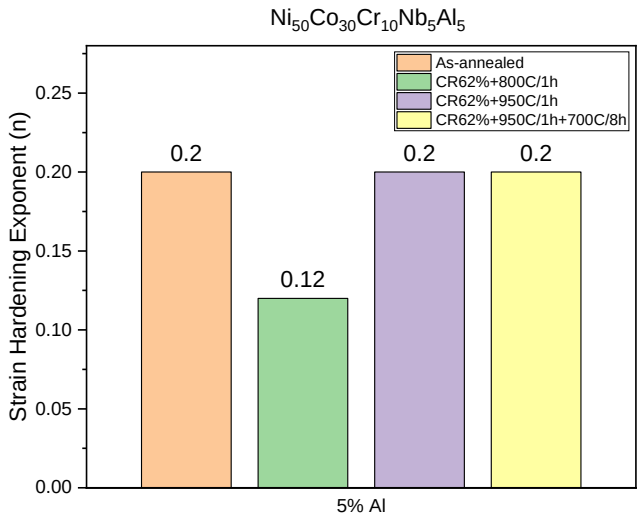

Figure 52: Strain hardening exponent of $Ni_{50}Co_{30}Cr_{10}Nb_5Al_5$ at all processing conditions.

The true uniform strain appeared to be the highest on the annealed and CR62%+950ºC/1h samples with values 42% and 30% respectively. As the 600 and 800 aged specimens showed low ductility and formability, the true uniform strain values did not exceed more that 2.6% as expressed in Figure 53. The CR62%+950ºC/1h+700ºC/8h showed 22.3% of uniform strain which observed to be high value for an alloy with superior strength.

From the above understanding and analysed mechanical properties, the CR62%+950ºC/1h+700ºC/8h sample can be selected as the best sample that provide unconventional mechanical properties, where its mechanical properties gave almost the

best results in all mechanical characteristics with a yield of 1170 MPa, 28.5% elongation to fracture, and almost a UTS of 1988 GPa. In addition, the two-step treatment condition can be selected as the best method for $Ni_{50}Co_{30}Cr_{10}Nb_5Al_5$ compared with the rest of applied conditions that have been examined, where this method joined the strength and ductility in a single alloy. In general, a yield strength of 1.1 GPa can be categorized as a yield strength for an advanced alloy which could be used in advanced applications such as gas turbines and aircraft engines. In comparing the mechanical properties of Inconel 718, the $Ni_{50}Co_{30}Cr_{10}Nb_5Al_5$ HEA with treatment CR62%+950ºC/1h+700ºC/8h produced much better mechanical properties than Inconel, except in ductility as the Inconel provide around 33% of elongation.

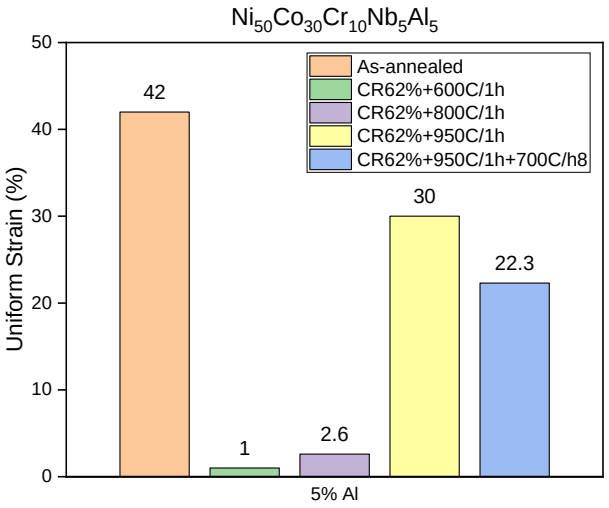

Figure 53: Uniform strain of $Ni_{50}Co_{30}Cr_{10}Nb_5Al_5$ at all processing methods.

4.2.3 Mechanical Properties of $Ni_{45}Co_{30}Cr_{10}Nb_5Al_{10}$ (10% Al)

The composition of this alloy concludes the mechanical properties at the highest aluminum concentration to the maximum level (10%). The true stress-strain curves in Figure 54 expressed the examined tensile samples at all processing conditions. The annealed sample showed the highest ductility of 34% with yield strength and ultimate tensile strength as 695 MPa and 1267 MPa respectively which observed later to be the

lowest values. The CR62%+600ºC/1h sample showed the lowest ductility of 0.98% beside 1507 MPa of yield strength and 1557 MPa of ultimate tensile strength where the sample fractured after very short range of yield point. In 800 ºC aging process, the ductility improved to 3.3% and the ultimate tensile strength increased to 1685 MPa, but it has been noticed that the yield strength decreased slightly to 1480 MPa.

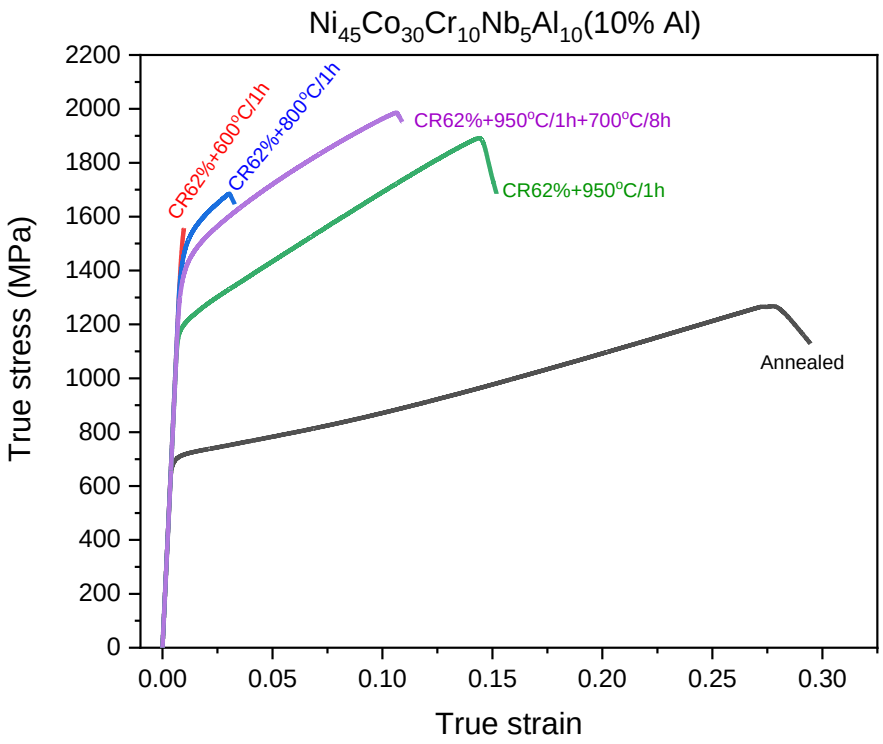

Figure 54: True stress-strain curves for $Ni_{45}Co_{30}Cr_{10}Nb_5Al_{10}$ at all processing methods.

The CR62%+950ºC/1h sample showed a significant enhancement in the mechanical properties with 16% ductility and 1891 MPa ultimate tensile strength. But this enhancement followed by a decrement in yield strength which measured as 1188 MPa. The CR62%+950ºC/1h+700ºC/8h sample has showed the most excellent results from strength respective with intermediate ductility, where the properties can be summarized as following: 1400 MPa of yield strength, 1986 MPa ultimate tensile strength and

11.5% of ductility. So, it can be observed that the two-step treatment succeeds in enhance both yield and ultimate tensile strengths with keeping the ductility more than 10%. The hardness results for all treatment methods were found between 4.1 and 6.4 as summarized in Figure 55 which confirmed the inverse relation between the hardness and aging temperature that already noticed in other compositions of 0% and 5% Al with an exception to the CR62%+950ºC/1h+700ºC/8h sample as it showed an enhancement in hardness to 5.5 GPa.

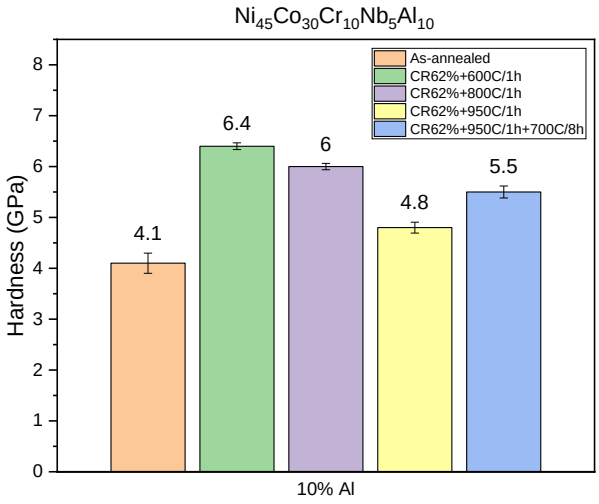

Figure 55: Hardness results for $Ni_{45}Co_{30}Cr_{10}Nb_5Al_{10}$ at all processing methods.

In fact, the ductility showed a proportional relation with aging temperature where the lowest values appeared in the 600ºC and 800ºC aged samples as 0.98% and 3.3% respectively. But it worth noting that the double heat treatment produced a reduction in ductility as it increases the hardness of the sample, but the ductility reduction where not significant and kept more than 10%.

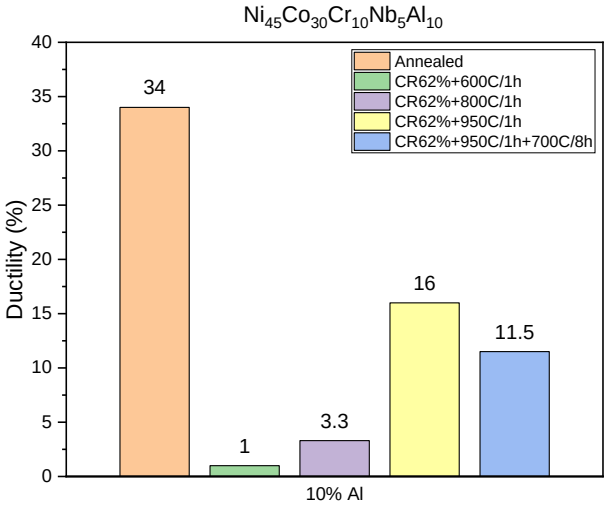

Figure 56: Ductility results for $Ni_{45}Co_{30}Cr_{10}Nb_5Al_{10}$ at all processing methods.

The yield strength of annealed sample found to be the lowest as 695 MPa. Then the 600 ºC and 800 ºC aged samples were recorded the greatest yield strengths of 1507 and 1480 MPa respectively. The 950 ºC aged sample showed a yield strength of 1188 MPa which is noted to be an excellent result in addition to its ductility and hardness which both were lay in the advance level. For CR62%+950ºC/1h+700ºC/8h sample, the yield strength had increased again to 1400 MPa after being decrease with the aging temperature. The yield strength values gave an inverse relation with the aging temperature whereas shown in Figure 57 the yield strength keeps decrease as the aging temperature increase until the two-step treatment which caused to increase the yield strength.

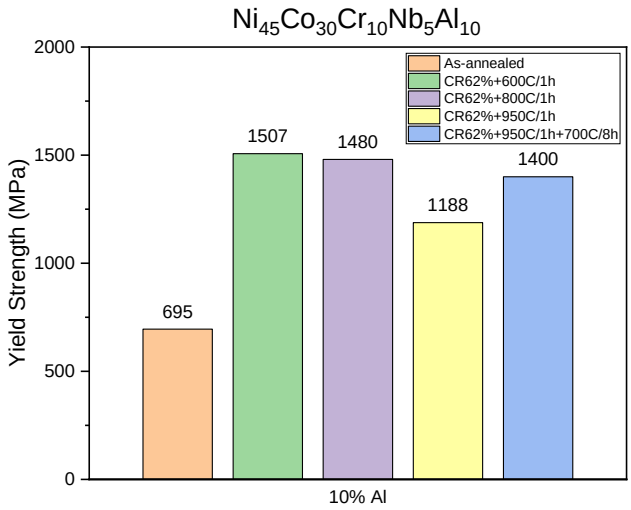

Figure 57: Yeild strength results of $Ni_{45}Co_{30}Cr_{10}Nb_5Al_{10}$ at all processing methods.

The ultimate tensile strength values showed a clear proportional relation with the aging temperature as presented in Figure 58 where the ultimate tensile strength point kept increase at all treatment conditions from annealing up to two-step treatment.

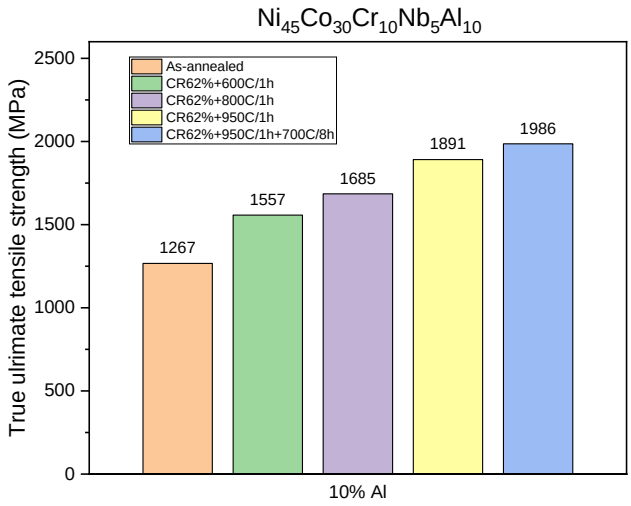

Figure 58: True ultimate tensile strength results of $Ni_{45}Co_{30}Cr_{10}Nb_5Al_{10}$ at all processing conditions.

By measuring the true uniform strain for all samples, it has been found that the highest values observed on annealed and 950 ºC aged samples as 31% and 15% respectively.

The lowest uniform strain results were found on 600 ºC and 800 ºC aged samples as 1% and 3% respectively, and this can be clarified due to their low ductility and formability where the fracture occurred after short range of yield point. The CR62%+950ºC/1h+700ºC/8h sample also showed a good result of 11%. In summary, the aging temperature demonstrated a proportional relationship with uniform strain values except at two-step treatment which exhibit a reduction in the uniform strain.

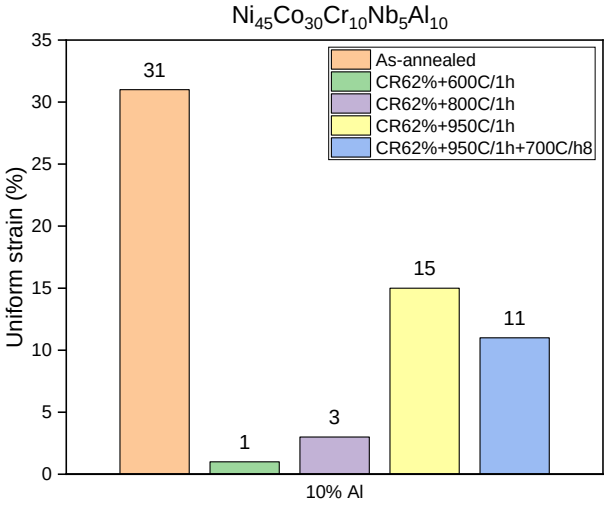

Figure 59: Uniform strain results of $Ni_{45}Co_{30}Cr_{10}Nb_5Al_{10}$ at all processing methods.

The strain hardening exponents briefed in Figure 60 for $Ni_{45}Co_{30}Cr_{10}Nb_5Al_{10}$ HEA at all processing conditions. The strain hardening exponent of 600 ºC aged sample was not calculated as the tensile sample fractured nearly at the yield point. The annealed and 950 ºC aged samples showed similar strain hardening exponents of 0.19 and 0.18 respectively and the CR62%+950ºC/1h+700ºC/8h sample exhibit 0.15 for strain hardening exponent. Due to its low ductility and formability, the 800 ºC aged sample gave the lowest strain hardening exponent of 0.1.

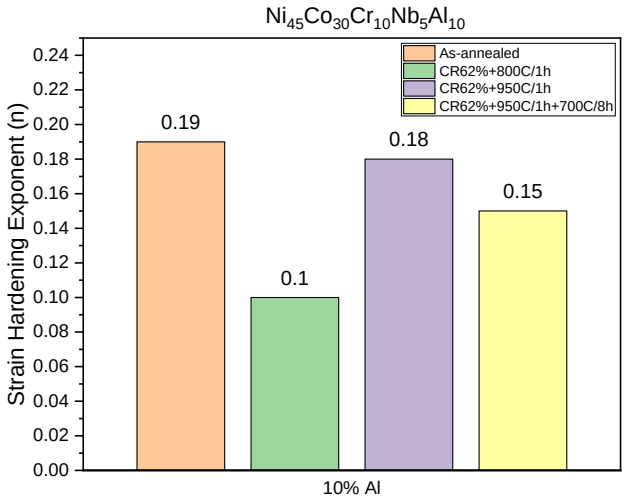

Figure 60: Strain hadening exponent results of $Ni_{45}Co_{30}Cr_{10}Nb_5Al_{10}$ at all processing methods.

4.2.4 Effect of Al Concentration on the Mechanical Properties

Table 2 is summarizing all obtained mechanical properties of the produced samples at each thermomechanical treatment condition. This table used to select the most excellent HEA and the optimum thermomechanical treatment for the HEAs.

Table 2: Summary of the Key Mechanical Properties of All Produced HEAs at All Thermomechanical Tertment Conditions. σ_y: Yeild Strength, σ_{UTS}: Ulimate Tensile Strength, Elongation, HR: Hardness and n: Strain Hardening Exponent.

Property	Annealed			Aged 600°C			Aged 800°C			Aged 950°C			Aged 950°C+700°C		
	0%Al	5%Al	10%Al	0%Al	5%Al	10%Al	0%A	5%Al	10%Al	0%Al	5%Al	10%Al	0%A	5%Al	10%Al
σ_y, MPa	291	840	695	1589	1812	1507	873	1650	1480	385	1014	1188	398	1170	1400
σ_{UTS}, MPa	967	1606	1267	1747	1898	1557	1382	1842	1685	1588	1875	1891	1607	1988	1986
Elongation,%	75	44	34	6.9	1	1	21	3.6	3.3	94	35	16	85.1	28.5	11.5
HR, GPa	2.4	4.3	4.1	4.6	6.8	6.4	3.3	4.4	6	2.6	4.3	4.8	2.6	5	5.5
n	0.34	0.2	0.19	0.05	…….	…….	0.15	0.12	0.1	0.4	0.2	0.18	0.39	0.2	0.15

The tested HEAs at all subjected processing conditions indicate that the two-step treatment (CR62%+950ºC/1h+700ºC/8h) is almost the best method of processing. So, the HEAs of 0%, 5% and 10% of Al that prepared through two-step treatment were

compared to each other as at the optimum treatment method and based on Al content variation. Figure 61 shows a comparison of Al concentration in NiCrCoNb HEA to the strength properties of yield strength, UTS, and fracture stress. The yield strength and fracture stress showed a clear proportional relation with Al concentration where the values kept increase as the Al percentage increase. The UTS exhibit to be the lowest at 0% Al and an almost similar UTS values appeared at 5 and 10% of Al.

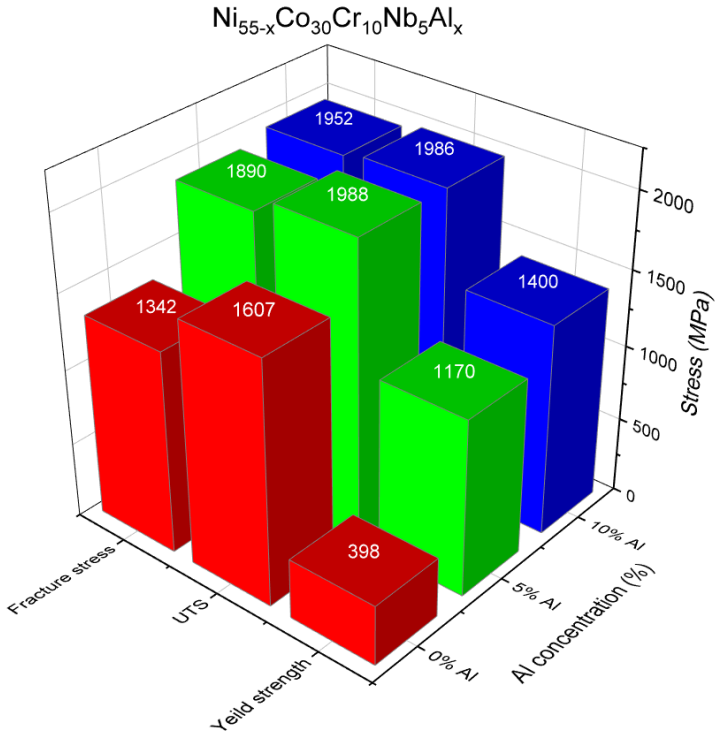

Figure 61: Strength properties versus Al percentage in $Ni_{55-x}Co_{30}Cr_{10}Nb_5Al_X$ HEA processed as CR62%+950ºC/1h+700ºC/8h.

The elongation properties of ductility and uniform strain had also compared in Figure 62 where both aspects showed a clear inverse relationship with Al concentration. The absence of Al in the composition cause to produce very high ductility and uniform strain and by increasing the Al to 5% the ductility lost more than 65% of its initial value. The elongation properties results from 10% Al confirmed the inverse relation of Al concentration with the elongation properties.

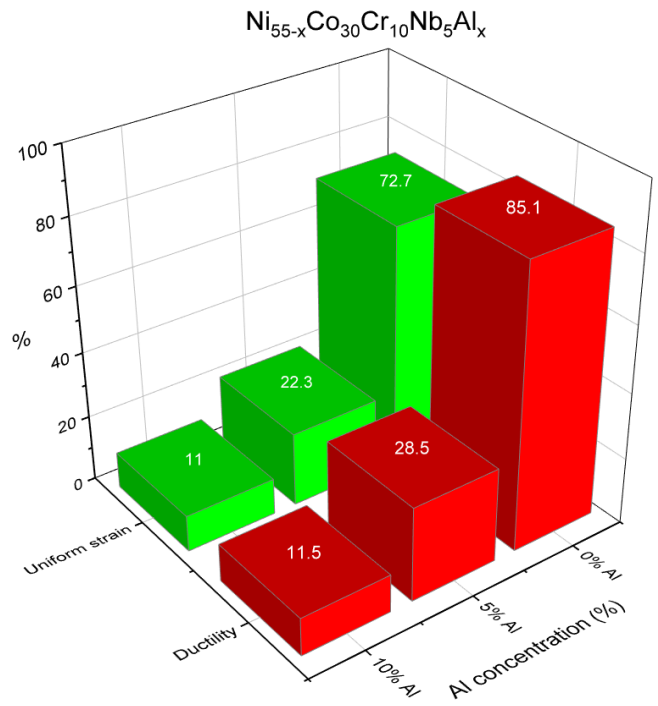

Figure 62: Elongation properties versus Al concentration in $Ni_{55-x}Co_{30}Cr_{10}Nb_5Al_X$ HEA processed as CR62%+950ºC/1h+700ºC/8h.

To compare our results with current market products, Inconel 718 had tested mechanically in the lab and compared with our work as shown in Figure 63. The yield strength of Inconel 718 measured as 943 MPa which much less than 5% and 10% and higher than 0%Al processed at CR62%+950ºC/1h+700ºC/8h. The UTS of Inconel 718 was recorded as 1563.9 MPa which found close to 0%Al UTS value. It's worth noting that Inconel 718 gave in the comparison to other HEAs the second highest ductility of 33.5% which overpass $Ni_{50}Co_{30}Cr_{10}Nb_5Al_5$ and $Ni_{45}Co_{30}Cr_{10}Nb_5Al_{10}$. The HEAs which contain 5% and 10% of Al were both presented the best strength properties, but the 10%Al did not provide a good elongation as 5%Al. So, in comparing the Inconel 718 with 5%Al, our results showed extremely better strength and with excellent ductility to let our work conclude the comparison view with Inconel 718 as the provided excessive mechanical features.

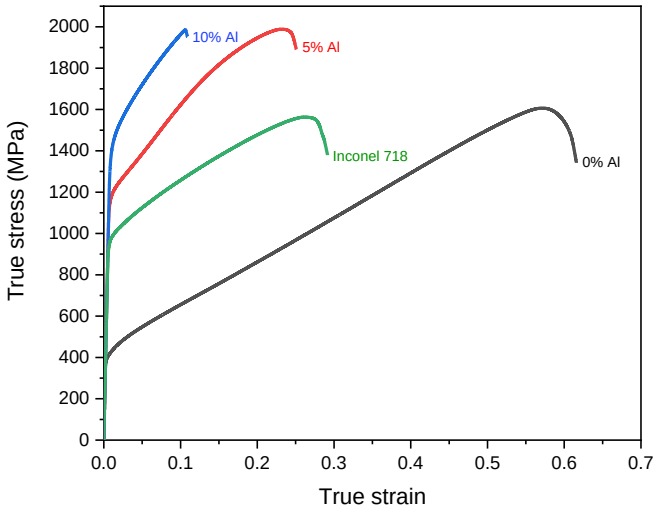

Figure 63: True stress-strain curve of $Ni_{55-x}Co_{30}Cr_{10}Nb_5Al_x$ procesed at double heat treatment process compared to Inconel 718.

The comparison view has been extended to reach other alloys and HEAs such as CoCrFeMnNi [70], $Al_{0.3}$CrCoFeNi [71], and dual phase HEAs [72]. From the previous understanding of the analyzed mechanical properties for the produced HEAs, all the data were compared to each other and to the results in literature by built a ductility versus UTS relation as shown in Figure 64 in order to have a modern assessment to the recent studies. The results of $Ni_{55}Co_{30}Cr_{10}Nb_5$ (0%Al) were mainly located around $Al_{0.3}$CoCrFeNi HEA with showing similar ductility and better UTS. The ductility-UTS major results of $Ni_{45}Co_{30}Cr_{10}Nb_5Al_{10}$ (10%Al) HEA demonstrated next to dual phase HEAs with better ultimate tensile strength values. The $Ni_{50}Co_{30}Cr_{10}Nb_5Al_5$ (5%Al) HEA appeared to be the best HEA compared to the subjected alloys in the graph, where it values located after dual phase HEAs, CoCrFeMnNi HEAs, and nanoprecipitate HEAs giving advanced values that join good ductility with high strength.

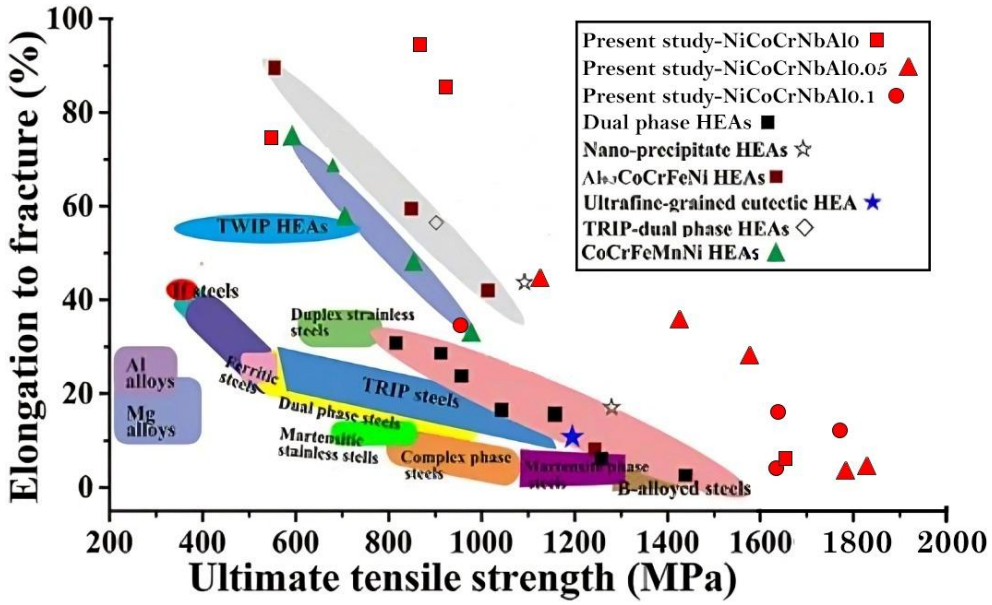

Figure 64: Ductility versus engineering UTS of different alloys and HEAs compared to our HEAs $Ni_{55}Co_{30}Cr_{10}Nb_5$, $Ni_{50}Co_{30}Cr_{10}Nb_5Al_5$, and $Ni_{45}Co_{30}Cr_{10}Nb_5Al_{10}$.

Additional HEAs have been added to the comparison study as presented in Table 3. It's clearly appeared that our HEAs showed better mechanical properties than CrMnFeCoNi [73], CrFeCoNiPd [55], CrMnFeCo [74], and CrCoNi [75] HEAs, where the highest UTS for those HEAs showed as 884 MPa which is less than the lowest than recorded UTS for NiCrCoNb. Also, the yield strength showed to be almost two time greater than the compared HEAs.

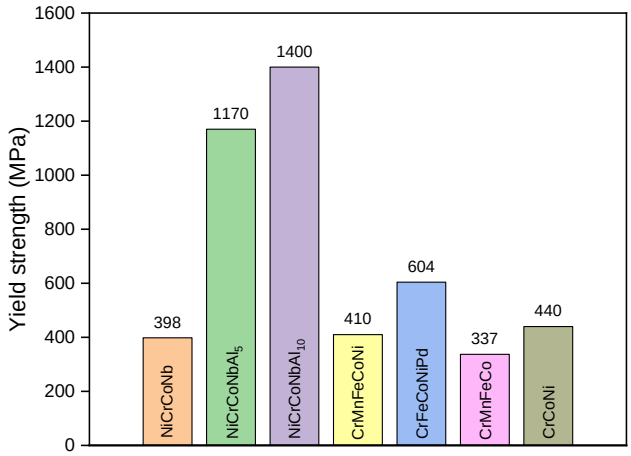

Figure 65: Comparison of yield strength between $Ni_{55-x}Co_{30}Cr_{10}Nb_5Al_x$ HEAs processed at 62%+950°C/1h+700°C/8h and other HEAs.

Table 3: Properties of the $Ni_{55-x}CrCoNbAl_x$ HEAs Processes at 62%+950°C/1h+700°C/8h Compared to CrMnFeCoNi [73], CrFeCoNiPd [55], CrMnFeCo [74] and CrCoNi [75] HEAs.

Alloy	Grain Size (µm)	σ_Y(MPa)	σ_{UTS}(MPa)	Ɛ (%)	n
$NiCoCrNbAl_0$	33.7	398	1607	85.1	0.39
$NiCoCrNbAl_5$	50.8	1170	1988	28.5	0.2
$NiCoCrNbAl_{10}$	n/a	1400	1986	11.5	0.15
CrMnFeCoNi	6	410	763	57	0.41
CrFeCoNiPd	5	604	835	44	0.38
CrMnFeCo	4.5	337	872	74	n/a
CrCoNi	5-50	440	884	73	0.4

4.3 Cost Analysis and Materials Availability

The price and cost of the raw elements is the main factor in making our HEAs a competitive product to the current options in the global market, where the price could

add an interesting advantage over the current choices especially in reducing the cost of manufacturing the products. FU at el. made an initial pricing summary for HEAs raw elements, where they categorized the elements into four main classes by averaging the prices of the elements to the last 50 years' data [76]. The prices were grouped in Table 4, where London Metal Exchange (LME) along with the United States Geological Survey (USGS) [77] had been used as the prices data source. Table 4, it is clearly shown that most of elements used in our study are between low and intermediate prices which made the cost of the entire alloy relatively low as the main contributed elements are lay on low price elements. In addition, 65% of the total weight for $NiCrCoNbAl_{0.05}$ HEA is laid at a low price class. In making a price comparison of the studied HEAs to the Inconel 718, which dominates the current market, our HEAs undoubtedly surpass the Inconel 718 from the cost point of view, where the absence of several elements such as Ti and Mo could effectively reduce the overall cost of our HEA.

Table 4: HEA Elements of the Last Decade in Terms of 50 Year Historic Average Price.

Elements Category	Elements	Price
Very high price	Au, Sc	>1000
High price	Ag, Ga, Ge, Hf, In, La, Ta	100
Intermediate price	Be, Bi, Cd, Co, Mo, Nb, Sn, Te, W, Y, Zr	5
Low price	Al, Cr, Cu, Fe, Li, Mg, Mn, Ni, Pb, Sb, Si, Ti, V, Zn	0.5

Some metals may not be easily available in the future due to the high extraction of raw material, and this risk has increased the interest in exploring material use and design [78], [79]. The threat of materials availability has been reported in several articles [80]–[82]. In addition, its dependency on several factors including geopolitical concentration, government stability, geological abundance, economic policy and substitution potential [80]. Fu at el. studied the materials availability risk by focus on

geopolitical supply concentration using the Herfindahl- Hirschman Index (HHI) in addition of consideration whether a given constituent element is mined as a byproduct [76]. The formula of Herfindahl-Hirschman Index is shown as the below, where "si" is the percent market share of country "i" compared to world production and M is the total number of countries involved.

$$\text{HHI} = \sum_{i}^{M} Si^2$$

According to the Federal Trade Commission and U.S. Department of Justice the markets considered to be highly concentrated' when HHI>2500, moderately concentrated when the HHI 1500-2500 and not concentrated when HHI<1500 [78], [79]. Figure 66 provides HHI indexing for 33 elements, where Ni, Cr and Al reported between low and medium HHI. Cobalt and Niobium had considered in the below graph as highly concentrated, especially Niobium which reported in top 10 highest HHI. But it's worth noting that Niobium is the lowest contributed elements in our HEAs with only 5% of the whole composition. Also, HHI represents only the risk from geopolitical supply concentration point of view, hence these numbers could be varied in case that the other factors considered.

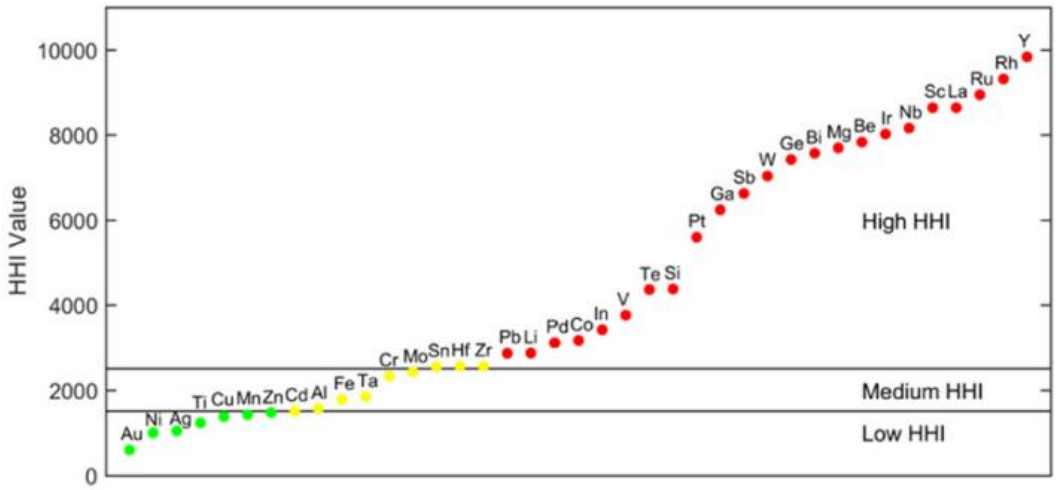

Figure 66: Herfindahl-Hirschman Index (HHI) for 33 different elements [76].

CHAPTER 5: CONCLUSION

The NiCoCrNb high entropy alloys had prepared and investigated in this thesis based on variation in aluminum content at 0%, 5% and 10%. The thermomechanical treatment processes were optimized, and the effect of Al content on the structural, phase stability, and mechanical properties were studied. The $Ni_{55}Co_{30}Cr_{10}Nb_5$ (0% Al) HEA provided relatively a low strength with high ductility due to the absence of aluminum in the chemical composition. The $Ni_{45}Co_{30}Cr_{10}Nb_5Al_{10}$ (10% Al) HEA provided a high strength at all thermomechanical treatments but with the lowest ductility values due to the high content of aluminum in the chemical composition which caused to produce uncrystallized structure after the thermomechanical processes. The $Ni_{50}Co_{30}Cr_{10}Nb_5Al_5$ (5% Al) HEA recorded the best combination of strength and ductility at most of thermomechanical treatment processes, where the 5% Al content provided excellent strengthening mechanisms of twinning, precipitates, and chemical short-range ordering (CSRO). The outstanding mechanical properties of $Ni_{50}Co_{30}Cr_{10}Nb_5Al_5$ HEA had elucidated through structural analysis of TEM, SEM, and EBSD. The mechanical properties, structural features, and effective cost of the $Ni_{50}Co_{30}Cr_{10}Nb_5Al_5$ HEA could conclude this study and make the $Ni_{50}Co_{30}Cr_{10}Nb_5Al_5$ HEA as the optimum HEA that produced with 5% Al concentration though several thermomechanical treatments. The thermomechanical treatment condition 62%+950ºC/1h+700ºC/8h showed the best treatment method for $Ni_{50}Co_{30}Cr_{10}Nb_5Al_5$ HEA by joining between superior strength and high ductility in a single alloy. The presence of CSRO in $Ni_{50}Co_{30}Cr_{10}Nb_5Al_5$ could refer as one of the main reasons of the superior mechanical results, especially that it has been reported in several studies as a strengthening factor in HEAs. Also, the observed Nb-rich precipitation at the grain boundaries played role in boosting the strength of the $Ni_{50}Co_{30}Cr_{10}Nb_5Al_5$ HEA, where these precipitates work as an obstacle during atomic

planes slip, providing unconventional fracture mechanism. In addition, the sharp reduction in $Ni_{50}Co_{30}Cr_{10}Nb_5Al_5$ grain size from 233.5µm to 50.8µm due to 62%+950ºC/1h+700ºC/8h thermomechanical treatment could be added to the high mechanical results reasons, where the more grain boundaries the more strength for material [69]. Moreover, the existence of twinning defect in $Ni_{50}Co_{30}Cr_{10}Nb_5Al_5$ HEA structure could be added as another reason for the obtained high mechanical properties. Furthermore, the $Ni_{50}Co_{30}Cr_{10}Nb_5Al_5$ HEA that processed at 62%+950ºC/1h+700ºC/8h got compared to Inconel 718 alloy from mechanical properties point of view, where that numbers indicated increments in yield strength by 24%, ultimate tensile strength by 27% and 37% in fracture stress. In the end, the mechanical properties of $Ni_{55-x}Co_{30}Cr_{10}Nb_5Al_x$ HEAs at treatment method 62%+950ºC/1h+700ºC/8h got compared to several HEAs and MEAs such as CrMnFeCoNi, CrFeCoNiPd, CrMnFeCo, and CrCoNi, where our results had overcome all these alloys, and none of the compared HEAs could join between ductility and strength as $Ni_{50}Co_{30}Cr_{10}Nb_5Al_5$ HEA.

CHAPTER 6: FUTURE WORK

After the extraordinary combination of strength and ductility of the investigated high entropy alloys, the discussion leads to several plans for future work to extend the analysis methods for advanced characterization to better understand the detailed micro-, nano-structure of these HEAs. Such alloys could be an excellent candidates for high strength at high-temperature applications. Thus, tensile properties at elevated temperatures would be of significant interest. It is also recommended to investigate the effect of low temperature on the mechanical behavior, especially it has been reported that the CrCoNi-based alloys display excellent mechanical properties particularly at low temperatures [73], [75]. Since the improvement in mechanical properties of HEAs and MEAs was reported to be highly linked with the chemical short-range ordering (CSRO) [64], [83]–[86], it is highly recommended to thoroughly investigate the CSRO effect in such HEAs. In addition, the thermomechanical treatment used in this thesis could be improved to produce better mechanical and structural properties, where many methods such as quenching, are still not tested in this study which might produce more significant outcomes. The recyclability of HEAs is another exciting feature, where it has been reported that HEAs could be more recyclable than conventional alloys [76]. From this point, the HEAs consisting of expensive elements might drive interest in recycling, since recovering expensive materials could add an economic benefit to the producers. Thus, the recyclability of the NiCrCoNbAl HEAs could be added to our future goals, which could add economic and environmental advantages to the production process.

REFERENCES

[1] J. W. Yeh *et al.*, “Nanostructured high-entropy alloys with multiple principal elements: Novel alloy design concepts and outcomes,” *Adv. Eng. Mater.*, vol. 6, no. 5, pp. 299–303, May 2004, doi: 10.1002/adem.200300567.

[2] B. Cantor, I. T. H. Chang, P. Knight, and A. J. B. Vincent, “Microstructural development in equiatomic multicomponent alloys,” *Mater. Sci. Eng. A*, vol. 375–377, no. 1-2 SPEC. ISS., pp. 213–218, Jul. 2004, doi: 10.1016/j.msea.2003.10.257.

[3] J. Chen *et al.*, “A review on fundamental of high entropy alloys with promising high–temperature properties,” *J. Alloys Compd.*, vol. 760, pp. 15–30, 2018, doi: 10.1016/j.jallcom.2018.05.067.

[4] F. J. Wang, Y. Zhang, G. L. Chen, and H. A. Davies, “Cooling rate and size effect on the microstructure and mechanical properties of AlCoCrFeNi high entropy alloy,” *J. Eng. Mater. Technol.*, vol. 131, no. 3, 2009.

[5] E. P. George, W. A. Curtin, and C. C. Tasan, “High entropy alloys: A focused review of mechanical properties and deformation mechanisms,” *Acta Mater.*, vol. 188, pp. 435–474, 2020, doi: 10.1016/j.actamat.2019.12.015.

[6] J. Chen *et al.*, “Effect of Zr content on microstructure and mechanical properties of AlCoCrFeNi high entropy alloy,” *Mater. Des.*, vol. 94, pp. 39–44, 2016.

[7] O. N. Senkov, J. M. Scott, S. V Senkova, F. Meisenkothen, D. B. Miracle, and C. F. Woodward, “Microstructure and elevated temperature properties of a refractory TaNbHfZrTi alloy,” *J. Mater. Sci.*, vol. 47, no. 9, pp. 4062–4074, 2012.

[8] N. Kumar, M. Fusco, M. Komarasamy, R. S. Mishra, M. Bourham, and K. L. Murty, “Understanding effect of 3.5 wt.% NaCl on the corrosion of Al0.

1CoCrFeNi high-entropy alloy," *J. Nucl. Mater.*, vol. 495, pp. 154–163, 2017.

[9] T. Tsao, A. Yeh, C. Kuo, and H. Murakami, "On the superior high temperature hardness of precipitation strengthened high entropy Ni-based alloys," *Adv. Eng. Mater.*, vol. 19, no. 1, p. 1600475, 2017.

[10] O. N. Senkov, G. B. Wilks, J. M. Scott, and D. B. Miracle, "Mechanical properties of Nb25Mo25Ta25W25 and V20Nb20Mo20Ta20W20 refractory high entropy alloys," *Intermetallics*, vol. 19, no. 5, pp. 698–706, 2011.

[11] Z. Li, A. Ludwig, A. Savan, H. Springer, and D. Raabe, "Combinatorial metallurgical synthesis and processing of high-entropy alloys," *J. Mater. Res.*, vol. 33, no. 19, pp. 3156–3169, 2018, doi: 10.1557/jmr.2018.214.

[12] S. Guo, C. Ng, J. Lu, and C. T. Liu, "Effect of valence electron concentration on stability of fcc or bcc phase in high entropy alloys," *J. Appl. Phys.*, vol. 109, no. 10, 2011, doi: 10.1063/1.3587228.

[13] F. Otto, Y. Yang, H. Bei, and E. P. George, "Relative effects of enthalpy and entropy on the phase stability of equiatomic high-entropy alloys," *Acta Mater.*, vol. 61, no. 7, pp. 2628–2638, Apr. 2013, doi: 10.1016/J.ACTAMAT.2013.01.042.

[14] P. Sharma, V. K. Dwivedi, and S. P. Dwivedi, "Development of high entropy alloys: A review," *Mater. Today Proc.*, vol. 43, pp. 502–509, 2020, doi: 10.1016/j.matpr.2020.12.023.

[15] D. B. Miracle and O. N. Senkov, "A critical review of high entropy alloys and related concepts," *Acta Mater.*, vol. 122, pp. 448–511, 2017, doi: 10.1016/j.actamat.2016.08.081.

[16] M. G. Poletti and L. Battezzati, "Electronic and thermodynamic criteria for the occurrence of high entropy alloys in metallic systems," *Acta Mater.*, vol. 75, pp.

297–306, 2014, doi: 10.1016/j.actamat.2014.04.033.

[17] M. H. Tsai and J. W. Yeh, “High-entropy alloys: A critical review,” *Mater. Res. Lett.*, vol. 2, no. 3, pp. 107–123, 2014, doi: 10.1080/21663831.2014.912690.

[18] Y. E. H. Jien-Wei, “Recent progress in high entropy alloys,” *Ann. Chim. Sci. Mat*, vol. 31, no. 6, pp. 633–648, 2006.

[19] L. S. Zhang, G. L. Ma, L. C. Fu, and J. Y. Tian, “Recent progress in high-entropy alloys,” *Adv. Mater. Res.*, vol. 631–632, pp. 227–232, 2013, doi: 10.4028/www.scientific.net/AMR.631-632.227.

[20] T. Saito *et al.*, “Multifunctional alloys obtained via a dislocation-free plastic deformation mechanism,” *Science (80-.).*, vol. 300, no. 5618, pp. 464–467, 2003, doi: 10.1126/science.1081957.

[21] A. Vazquez and S. K. Varma, “High-temperature oxidation behavior of Nb-Si-Cr alloys with Hf additions,” *J. Alloys Compd.*, vol. 509, no. 25, pp. 7027–7033, Jun. 2011, doi: 10.1016/j.jallcom.2011.02.174.

[22] C. Wen *et al.*, “Machine learning assisted design of high entropy alloys with desired property,” *Acta Mater.*, vol. 170, pp. 109–117, 2019, doi: 10.1016/j.actamat.2019.03.010.

[23] S. Li, S. Li, D. Liu, R. Zou, and Z. Yang, “Hardness prediction of high entropy alloys with machine learning and material descriptors selection by improved genetic algorithm,” *Comput. Mater. Sci.*, vol. 205, no. September 2021, p. 111185, 2022, doi: 10.1016/j.commatsci.2022.111185.

[24] G. Vazquez *et al.*, “Efficient machine-learning model for fast assessment of elastic properties of high-entropy alloys,” *Acta Mater.*, vol. 232, p. 117924, 2022, doi: 10.1016/j.actamat.2022.117924.

[25] O. N. Senkov, J. M. Scott, S. V. Senkova, D. B. Miracle, and C. F. Woodward,

"Microstructure and room temperature properties of a high-entropy TaNbHfZrTi alloy," *J. Alloys Compd.*, vol. 509, no. 20, pp. 6043–6048, 2011, doi: 10.1016/j.jallcom.2011.02.171.

[26] H. Song *et al.*, "Local lattice distortion in high-entropy alloys," *Phys. Rev. Mater.*, vol. 1, no. 2, pp. 1–8, 2017, doi: 10.1103/PhysRevMaterials.1.023404.

[27] K. Y. Tsai, M. H. Tsai, and J. W. Yeh, "Sluggish diffusion in Co-Cr-Fe-Mn-Ni high-entropy alloys," *Acta Mater.*, vol. 61, no. 13, pp. 4887–4897, Aug. 2013, doi: 10.1016/j.actamat.2013.04.058.

[28] J. Y. He *et al.*, "Effects of Al addition on structural evolution and tensile properties of the FeCoNiCrMn high-entropy alloy system," *Acta Mater.*, vol. 62, no. 1, pp. 105–113, 2014, doi: 10.1016/j.actamat.2013.09.037.

[29] J. W. Yeh *et al.*, "Nanostructured high-entropy alloys with multiple principal elements: Novel alloy design concepts and outcomes," *Adv. Eng. Mater.*, vol. 6, no. 5, pp. 299–303, May 2004, doi: 10.1002/adem.200300567.

[30] C. C. Tung, J. W. Yeh, T. tsung Shun, S. K. Chen, Y. S. Huang, and H. C. Chen, "On the elemental effect of AlCoCrCuFeNi high-entropy alloy system," *Mater. Lett.*, vol. 61, no. 1, pp. 1–5, 2007, doi: 10.1016/j.matlet.2006.03.140.

[31] H.-P. Chou, Y.-S. Chang, S.-K. Chen, and J.-W. Yeh, "Microstructure, thermophysical and electrical properties in AlxCoCrFeNi ($0 \leq x \leq 2$) high-entropy alloys," *Mater. Sci. Eng. B*, vol. 163, no. 3, pp. 184–189, 2009.

[32] C. J. Tong *et al.*, "Mechanical performance of the AlxCoCrCuFeNi high-entropy alloy system with multiprincipal elements," *Metall. Mater. Trans. A Phys. Metall. Mater. Sci.*, vol. 36, no. 5, pp. 1263–1271, 2005, doi: 10.1007/s11661-005-0218-9.

[33] T. T. Shun and Y. C. Du, "Microstructure and tensile behaviors of FCC

Al0.3CoCrFeNi high entropy alloy," *J. Alloys Compd.*, vol. 479, no. 1–2, pp. 157–160, 2009, doi: 10.1016/j.jallcom.2008.12.088.

[34] Y. Zhang, C. C. Koch, S. G. Ma, H. Zhang, and Y. Pan, *Fabrication routes*. 2016.

[35] F. Wang, Y. Zhang, G. Chen, and H. A. Davies, "Tensile and compressive mechanical behavior of a CoCrCuFeNiAl0.5 high entropy alloy," *Int. J. Mod. Phys. B*, vol. 23, no. 6–7, pp. 1254–1259, 2009, doi: 10.1142/s0217979209060774.

[36] P. F. Yu *et al.*, "Effects of high pressure torsion on microstructures and properties of an Al0. 1CoCrFeNi high-entropy alloy," *Mater. Sci. Eng. A*, vol. 655, pp. 283–291, 2016.

[37] J. W. Yeh, S. K. Chen, and S. J. Lin, "with multiple principal elements: Nanoslruetured high-entropy alloys novel alloy design eoneepls and outcomes," *Advaneed Eng. Mater.*, vol. 6, no. 5, pp. 299–303, 2004.

[38] Y. Zhang *et al.*, "Metallurgical and materials Transactions A," *Metall. Mater. Trans.*, no. January 2020, 2020.

[39] F. Otto, A. Dlouhý, C. Somsen, H. Bei, G. Eggeler, and E. P. George, "The influences of temperature and microstructure on the tensile properties of a CoCrFeMnNi high-entropy alloy," *Acta Mater.*, vol. 61, no. 15, pp. 5743–5755, 2013.

[40] P. C. Gasson, "The Superalloys: Fundamentals and Applications RC Reed Cambridge University Press, The Edinburgh Building, Shaftesbury Road, Cambridge, CB2 2RU, UK, 2006. 372pp. Illustrated.£ 80. ISBN 0-521-85904-2.," *Aeronaut. J.*, vol. 112, no. 1131, p. 291, 2008.

[41] H. M. Daoud, A. M. Manzoni, N. Wanderka, and U. Glatzel, "High-temperature

tensile strength of Al10Co25Cr8Fe15Ni36Ti6 compositionally complex alloy (high-entropy alloy)," *Jom*, vol. 67, no. 10, pp. 2271–2277, 2015.

[42] Y. Y. Chen, T. Duval, U. D. Hung, J. W. Yeh, and H. C. Shih, "Microstructure and electrochemical properties of high entropy alloys-a comparison with type-304 stainless steel," *Corros. Sci.*, vol. 47, no. 9, pp. 2257–2279, Sep. 2005, doi: 10.1016/j.corsci.2004.11.008.

[43] Y. J. Hsu, W. C. Chiang, and J. K. Wu, "Corrosion behavior of FeCoNiCrCux high-entropy alloys in 3.5% sodium chloride solution," *Mater. Chem. Phys.*, vol. 92, no. 1, pp. 112–117, 2005, doi: 10.1016/j.matchemphys.2005.01.001.

[44] C. M. Lin and H. L. Tsai, "Evolution of microstructure, hardness, and corrosion properties of high-entropy Al0.5CoCrFeNi alloy," *Intermetallics*, vol. 19, no. 3, pp. 288–294, 2011, doi: 10.1016/j.intermet.2010.10.008.

[45] C. P. Lee, C. C. Chang, Y. Y. Chen, J. W. Yeh, and H. C. Shih, "Effect of the aluminium content of AlxCrFe1.5MnNi0.5 high-entropy alloys on the corrosion behaviour in aqueous environments," *Corros. Sci.*, vol. 50, no. 7, pp. 2053–2060, 2008, doi: 10.1016/j.corsci.2008.04.011.

[46] R. W. Cahn and P. Haasen, *Physical metallurgy*, vol. 1. Elsevier, 1996.

[47] K. Guruvidyathri, M. Vaidya, and B. S. Murty, "Challenges in design and development of high entropy alloys: A thermodynamic and kinetic perspective," *Scr. Mater.*, vol. 188, pp. 37–43, 2020, doi: 10.1016/j.scriptamat.2020.06.060.

[48] R. A. Swalin and J. Arents, "Thermodynamics of solids," *J. Electrochem. Soc.*, vol. 109, no. 12, p. 308C, 1962.

[49] K. Guruvidyathri, B. S. Murty, J. W. Yeh, and K. C. H. Kumar, "Gibbs energy-composition plots as a tool for high-entropy alloy design," *J. Alloys Compd.*, vol. 768, pp. 358–367, 2018.

[50] Y. Zhang, Y. J. Zhou, J. P. Lin, G. L. Chen, and P. K. Liaw, “Solid-solution phase formation rules for multi-component alloys,” *Adv. Eng. Mater.*, vol. 10, no. 6, pp. 534–538, 2008, doi: 10.1002/adem.200700240.

[51] X. Yang and Y. Zhang, “Prediction of high-entropy stabilized solid-solution in multi-component alloys,” *Mater. Chem. Phys.*, vol. 132, no. 2–3, pp. 233–238, 2012, doi: 10.1016/j.matchemphys.2011.11.021.

[52] Y. Zhang *et al.*, “Guidelines in predicting phase formation of high-entropy alloys,” *MRS Commun.*, vol. 4, no. 2, pp. 57–62, 2014, doi: 10.1557/mrc.2014.11.

[53] J. S. Benjamin, “Dispersion strengthened superalloys by mechanical alloying,” *Metall. Trans.*, vol. 1, no. 10, pp. 2943–2951, 1970, doi: 10.1007/BF03037835.

[54] “EBSD - Electron Backscatter Diffraction - Nanoanalysis - Oxford Instruments.” https://nano.oxinst.com/products/ebsd/ (accessed Jul. 15, 2022).

[55] Q. Ding *et al.*, “Tuning element distribution, structure and properties by composition in high-entropy alloys,” *Nature*, vol. 574, no. 7777, pp. 223–227, 2019, doi: 10.1038/s41586-019-1617-1.

[56] Y. F. Ye *et al.*, “Atomic-scale distorted lattice in chemically disordered equimolar complex alloys,” *Acta Mater.*, vol. 150, pp. 182–194, 2018, doi: 10.1016/j.actamat.2018.03.008.

[57] L. Zhang, Y. Xiang, J. Han, and D. J. Srolovitz, “The effect of randomness on the strength of high-entropy alloys,” *Acta Mater.*, vol. 166, pp. 424–434, 2019, doi: 10.1016/j.actamat.2018.12.032.

[58] Q. F. He, Y. F. Ye, and Y. Yang, “The configurational entropy of mixing of metastable random solid solution in complex multicomponent alloys,” *J. Appl. Phys.*, vol. 120, no. 15, 2016, doi: 10.1063/1.4965701.

[59] Q. F. He, Y. F. Ye, and Y. Yang, “Formation of Random Solid Solution in Multicomponent Alloys: from Hume-Rothery Rules to Entropic Stabilization,” *J. Phase Equilibria Diffus.*, vol. 38, no. 4, pp. 416–425, 2017, doi: 10.1007/s11669-017-0560-9.

[60] D. Liu *et al.*, “Chemical short-range order in Fe50Mn30Co10Cr10 high-entropy alloy,” *Mater. Today Nano*, vol. 16, 2021, doi: 10.1016/j.mtnano.2021.100139.

[61] M. C. Gao and D. E. Alman, “Searching for Next Single-Phase High-Entropy Alloy Compositions,” *Entropy*, vol. 15, no. 10, pp. 4504–4519, 2013, doi: 10.3390/e15104504.

[62] P. Singh, A. V. Smirnov, and D. D. Johnson, “Atomic short-range order and incipient long-range order in high-entropy alloys,” *Phys. Rev. B - Condens. Matter Mater. Phys.*, vol. 91, no. 22, pp. 1–12, 2015, doi: 10.1103/PhysRevB.91.224204.

[63] W. R. Jian, Z. Xie, S. Xu, Y. Su, X. Yao, and I. J. Beyerlein, “Effects of lattice distortion and chemical short-range order on the mechanisms of deformation in medium entropy alloy CoCrNi,” *Acta Mater.*, vol. 199, pp. 352–369, Oct. 2020, doi: 10.1016/J.ACTAMAT.2020.08.044.

[64] Q. J. Li, H. Sheng, and E. Ma, “Strengthening in multi-principal element alloys with local-chemical-order roughened dislocation pathways,” *Nat. Commun.*, vol. 10, no. 1, pp. 1–11, 2019, doi: 10.1038/s41467-019-11464-7.

[65] S. Guo *et al.*, “Overcoming strength-ductility trade-off in high-entropy alloys by tuning chemical short-range order and grain size,” *Intermetallics*, vol. 150, no. August, p. 107693, 2022, doi: 10.1016/j.intermet.2022.107693.

[66] S. Guo, H. Chen, and M. Wang, “Research on the dislocation differences of CoCrFeMnNi with different local chemical orders during room temperature

tensile test," *J. Alloys Compd.*, vol. 868, Jul. 2021, doi: 10.1016/J.JALLCOM.2021.159215.

[67] X. Yan, P. K. Liaw, and Y. Zhang, "Ultrastrong and ductile BCC high-entropy alloys with low-density via dislocation regulation and nanoprecipitates," *J. Mater. Sci. Technol.*, vol. 110, pp. 109–116, 2022, doi: 10.1016/j.jmst.2021.08.034.

[68] M. S. Moats and W. G. Davenport, *Nickel and Cobalt Production*, vol. 3. Elsevier Ltd., 2014.

[69] B. W. Inc, "Grain Size and Material Strength."

[70] S. J. Sun *et al.*, "Enhanced strength and ductility of bulk CoCrFeMnNi high entropy alloy having fully recrystallized ultrafine-grained structure," *Mater. Des.*, vol. 133, pp. 122–127, 2017, doi: 10.1016/j.matdes.2017.07.054.

[71] H. Y. Yasuda, H. Miyamoto, K. Cho, and T. Nagase, "Formation of ultrafine-grained microstructure in Al0.3CoCrFeNi high entropy alloys with grain boundary precipitates," *Mater. Lett.*, vol. 199, pp. 120–123, 2017, doi: 10.1016/j.matlet.2017.04.072.

[72] J. Hou, X. Shi, J. Qiao, Y. Zhang, P. K. Liaw, and Y. Wu, "Ultrafine-grained dual phase Al0.45CoCrFeNi high-entropy alloys," *Mater. Des.*, vol. 180, 2019, doi: 10.1016/j.matdes.2019.107910.

[73] B. Gludovatz, A. Hohenwarter, D. Catoor, E. H. Chang, E. P. George, and R. O. Ritchie, "A fracture-resistant high-entropy alloy for cryogenic applications," *Science (80-.).*, vol. 345, no. 6201, pp. 1153–1158, 2014, doi: 10.1126/science.1254581.

[74] Z. Li, K. G. Pradeep, Y. Deng, D. Raabe, and C. C. Tasan, "Metastable high-entropy dual-phase alloys overcome the strength-ductility trade-off," *Nature*,

vol. 534, no. 7606, pp. 227–230, 2016, doi: 10.1038/nature17981.

[75] B. Gludovatz *et al.*, “Exceptional damage-tolerance of a medium-entropy alloy CrCoNi at cryogenic temperatures,” *Nat. Commun.*, vol. 7, pp. 1–8, 2016, doi: 10.1038/ncomms10602.

[76] X. Fu, C. A. Schuh, and E. A. Olivetti, “Materials selection considerations for high entropy alloys,” *Scr. Mater.*, vol. 138, pp. 145–150, 2017, doi: 10.1016/j.scriptamat.2017.03.014.

[77] B. D. Thomas Kelly, G. R. Matos, with A. major contributions provided by David Buckingham, and C. A. DiFrancesco, “Historical Statistics for Mineral Commodities in the United States, Data Series 2005-140 U.S. Geological Survey Data Series 140 Historical Statistics for Mineral and Material Commodities in the United States Version 2.0 Online Only General Notes Methodology Commodity Data and Notes Reference,” Accessed: Sep. 24, 2022. [Online]. Available: http://minerals.usgs.gov/ds/2005/140/.

[78] L. Ghadbeigi, J. K. Harada, B. R. Lettiere, and T. D. Sparks, “Performance and resource considerations of Li-ion battery electrode materials,” *Energy Environ. Sci.*, vol. 8, no. 6, pp. 1640–1650, Jun. 2015, doi: 10.1039/C5EE00685F.

[79] M. W. Gaultois, T. D. Sparks, C. K. H. Borg, R. Seshadri, W. D. Bonificio, and D. R. Clarke, “Data-driven review of thermoelectric materials: Performance and resource onsiderations,” *Chem. Mater.*, vol. 25, no. 15, pp. 2911–2920, Aug. 2013, doi: 10.1021/CM400893E/ASSET/IMAGES/MEDIUM/CM-2013-00893E_0009.GIF.

[80] T. E. Graedel, E. M. Harper, N. T. Nassar, P. Nuss, B. K. Reck, and B. L. Turner, “Criticality of metals and metalloids,” *Proc. Natl. Acad. Sci. U. S. A.*, vol. 112, no. 14, pp. 4257–4262, Apr. 2015, doi:

10.1073/PNAS.1500415112/SUPPL_FILE/PNAS.1500415112.SAPP.PDF.

[81] M. Buchert, D. Schüler, and D. Bleher, “CritiCal metals for fUtUre sUstainable teChnologies and their reCyCling Potential Sustainable Innovation and Technology Transfer Industrial Sector Studies.”

[82] T. E. Graedel *et al.*, “Methodology of metal criticality determination,” *Environ. Sci. Technol.*, vol. 46, no. 2, pp. 1063–1070, Jan. 2012, doi: 10.1021/ES203534Z/SUPPL_FILE/ES203534Z_SI_001.PDF.

[83] C. G. Schön, “On short-range order strengthening and its role in high-entropy alloys,” *Scr. Mater.*, vol. 196, 2021, doi: 10.1016/j.scriptamat.2021.113754.

[84] J. Ding, Q. Yu, M. Asta, and R. O. Ritchie, “Tunable stacking fault energies by tailoring local chemical order in CrCoNi medium-entropy alloys,” *Proc. Natl. Acad. Sci. U. S. A.*, vol. 115, no. 36, pp. 8919–8924, 2018, doi: 10.1073/pnas.1808660115.

[85] F. X. Zhang *et al.*, “Local Structure and Short-Range Order in a NiCoCr Solid Solution Alloy,” *Phys. Rev. Lett.*, vol. 118, no. 20, pp. 1–6, 2017, doi: 10.1103/PhysRevLett.118.205501.

[86] W. R. Jian, Z. Xie, S. Xu, Y. Su, X. Yao, and I. J. Beyerlein, “Effects of lattice distortion and chemical short-range order on the mechanisms of deformation in medium entropy alloy CoCrNi,” *Acta Mater.*, vol. 199, pp. 352–369, 2020, doi: 10.1016/j.actamat.2020.08.044.